CIMAT

Numerical Solution of the Inverse Scattering Problem using High Level Representations

Thesis for the degree of **Doctor of Science**

with Specialization in Applied Mathematics

by

María Luisa Daza Torres

December 2017

Guanajuato, Guanajuato, México.

Advisor: Dr. Marcos Capistrán Ocampo.

This thesis is dedicated to your memory, my dear husband. For your infinite love, for being my support, for believing in me and my dreams, for always giving me wings to continue, for those wonderful years with you,

... and for that phrase, *eso es tuyo*.

Acknowledgements

I would like to express my sincere gratitude to my supervisor Marcos Capistrán, for his dedication, commitment, and perseverance with this work. His support and confidence motivated me every day to be my best version. I also want to thank Dr. Andrés Christen for his support, corrections, and collaboration.

Part of this thesis work was done while I was visiting Spain, where I received a warm welcome from Juan Antonio Infante. Thank you very much for your corrections and for believing in this work.

I am grateful to CONACYT which funded this work during these four years, and to CIMAT for its academic and economic support. Thanks also, to the Complutense University of Madrid for its hospitality.

Thanks to my friends Hireke, Verónica, Yury, and Lily to make life enjoyable even in those times when everything was dark. Thanks for those long conversations about the life, laughter, biking days, good food and above all for their support.

I am extremely grateful to have the love and unfaltering support of my Mexican family: Sebastián, Blanca, Éder, and Hireke. Thanks for everything, without you it would not have been possible.

Most of all, I am deeply grateful to my parents, Lancaster and Negia. They taught me to follow my dreams, and always to believe in me. Their love and support have been a great strength to me. Thanks also, to my sisters Susana, Aura, and Wendy for all their care and infinite love. They are my greatest motivation.

Finally, thank all those who in some way were part of this work.

Abstract

In this thesis, we consider the inverse scattering problem of reconstructing a penetrable homogeneous obstacle from near-field measurements of a scattered wave in 2D. This classical inverse scattering problem is challenging because it is both, ill-posed and nonlinear. On the other hand, since data is polluted with noise, the inverse problem may be regarded as a statistical inference problem. Consequently, we have opted for a Bayesian inferential framework. The Bayesian approach has allowed us to introduce a priori knowledge about the nature of the scatterer, i.e., we assume a star-shaped obstacle with constant refractive index. We rely on Markov Chain Monte Carlo (MCMC) methods to explore the arising posterior distribution. Each sample from the posterior distribution requires the solution of the direct problem, which is equivalent to integrating the Lippmann-Schwinger equation on the support of an approximating scatterer. We approximate the support of the scattering obstacle using a point cloud, which is a high-level representation. Of note, high-level representations are a well established topic of computational geometry. Our motivation to use high-level representations is two-fold: in the one hand, the direct problem has a threshold property, i.e., the derivative of the direct problem can be arbitrarily approximated by a finite rank operator, giving rise

to a low dimensional data-informed subspace. On the other hand, high level representations are intrinsically low dimensional, i.e. we design a suitable low dimensional parameter space to make inference easier.

In this thesis, we have introduced an efficient method to solve the Lippmann-Schwinger equation and a probability transition kernel that commutes with affine transformations of space to sample the posterior distribution. We offer numerical evidence of the following facts: First, we can recover simultaneously both, the (non)convex support of a star-shaped scattering obstacle and its constant refractive index. Second, we show that the MCMC separates the multiple scales of the inverse problem. Indeed, the MCMC first locates the position of the scatterer, and adjusts the shape and refractive index afterwards. We believe that our methods can be extended to multifrequency data.

Contents

List of Figures

List of Algorithms

Chapter 1

Introduction

Most of the information that we receive from physical reality comes through waves [72], e.g., acoustics, electromagnetics, geophysics, etc. Consequently, it is of paramount importance to develop mathematical methods to compute, explore and analyze wave phenomena. In particular, we need reliable methods to probe physical systems through scattering phenomena.

Indeed, scattering phenomena represents the most widely used mathematical model to recover unknown physical, geophysical, or medical objects from exterior observations [50, 44, 22]. These problems are fundamental in a wide range of applications such as medical imaging, materials engineering, geophysical explorations, nuclear energy, among others [4, 30, 67, 84, 54, 73, 76]. In a broad sense, scattering problems study the effect of an obstacle on an incident field.

In this work, the direct scattering problem consists of computing the scattered field given the incident field and the differential equations governing the wave motion. On the other hand, the inverse scattering problem requires estimating a feature (size, shape and refractive index) of the scatterer, from knowledge of the scattered field.

The inverse scattering problem, as defined above, is particularly difficult to solve for two reasons: it is (1) nonlinear and (2) ill-posed [23]. A number of numerical methods have been proposed to overcome these issues. They can be broadly classified into two categories: nonlinear optimization based iterative methods and imaging based direct methods. The iterative methods require good initial guesses and are computationally expensive. The direct methods are computationally efficient, but are qualitative in nature [59].

In the presence of noisy data, the mapping between unknown parameters and data is probabilistic; the inverse problem is a problem in statistical inference. Bayesian inferential methods offer solutions taking into account the stochastic structure of data, and the uncertainty on the parameters to be inferred [78]. Of note, the Bayesian formulation has been used as a paradigm for both, the solution of the inverse problem and the uncertainty quantification of model parameters [16, 81, 26, 28, 17, 34, 82, 48]. In this thesis, we care about the robust reconstruction of the obstacle and the refractive index, consequently, we have used the Bayesian framework.

The forward problem is modeled through of the Lippmann-Schwinger equation. This integral equation is approximated using a corrected trapezoidal rule [2] and the method of Vainikko [85]. A low-dimensional representation of the obstacle is posed using a point cloud. Initially, we approach the case of convex obstacles. Later, the formulation is extended to star-shaped obstacles using an α- shape algorithm [31].

The Markov Chain Monte Carlo (MCMC) with Metropolis-Hastings (MH) algorithm is applied to the exploration of the posterior probability distribution. Affine invariant proposals in the Metropolis-Hastings algorithm are used to guarantee efficiency [21, 38, 29]. The suitability of the proposed MCMC sampler is verified for several reconstruction examples using synthetic near-field data.

The thesis is organized as follows:

In Chapter II, the forward mapping is defined as the solution of Lippmann-Schwinger equation [23], and we present two numerical methods to approximate its solution. A high-level representation of the obstacle is detailed, the inverse scattering problem is formulated in the Bayesian framework, and we introduce an affine invariant Markov Chain Monte Carlo method to sample the arising posterior distribution.

In Chapter III, several numerical examples are proposed to show the performance of our approach using synthetic near-field data.

In Chapter IV, the numerical results are discussed, and the contributions of this thesis are summarized.

This thesis comprises scientific work; one paper published by the author.

Daza, Maria L., et al. "Solution of the inverse scattering problem from inhomogeneous media using affine invariant sampling." Mathematical Methods in the Applied Sciences 40.9 (2017): 3311-3319.

In this paper, it is tackled a classical inverse scattering problem: to estimate the support and refractive index of a scatterer given near-field measurements of scattered waves. It is posed a Bayesian formulation of the problem and introduced a transition kernel that is invariant under affine transformations of space. The support of the obstacle is approximated using a point cloud. The main contribution of the paper is that we offer evidence that it is possible to sample efficiently from the arising multiscale posterior distribution.

Chapter 2

Theoretical Framework

In this chapter, it is set each step to solve the inverse scattering problem in the Bayesian framework. The chapter is structured as follows: in section 2.1, the direct scattering problem is defined as the solution of the Helmholtz equation with a variable index of refraction. This problem is equivalent to the Lippmann-Schwinger equation. In section 2.1, two numerical methods to solve the Lippmann-Schwinger equation are presented. The above results thus enable us to define an operator $\mathbf{F}$ mapping the scattering obstacle and the refractive index onto the scattered field. In section 2.2, a representation of the obstacle based on a point cloud is explained. Employing the above results, in section 2.3, the inverse scattering problem is formulated in the Bayesian setting. The solution of the inverse problem is the posterior probability distribution. Thereby, in section 2.4 an affine invariant Markov Chain Monte Carlo (MCMC) to sample the posterior distribution is designed.

2.1 Scattering Problem

In this section, the direct scattering problem of incident time-harmonic plane waves in an inhomogeneous medium is established. In this case, the governing equation is the Helmholtz equation with an outgoing radiation condition, which is equivalent to the Lippmann-Schwinger equation. An efficient numerical method to approximate the Lippmann-Schwinger equation using corrected

trapezoidal rule is introduced. The efficiency of the indicated numerical method is exhibited using a benchmark.

2.1.1 Helmholtz Equation

Let consider a time-harmonic wave u^i that travels through an inhomogeneous acoustic medium, the wave is scattered by a penetrable obstacle of refractive index $b(x)$. The medium is represented by the space $\mathbb{R}^2$ and the scattering obstacle by the compact subset $D \subset R^2$ with boundary ∂D.

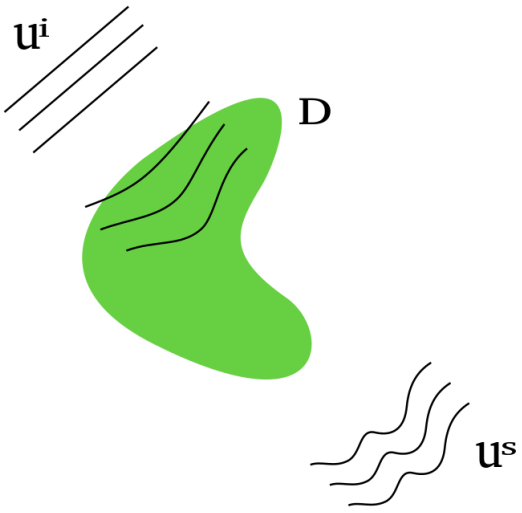

Figure 2.1: Scattering Problem.

Given the scatterer $D \subset \mathbb{R}^2$, the refractive index $b(x)$, and the incident plane wave u^i, the scattering problem consists of determining the total field $u = u^i + u^s$ as a solution of

$$\begin{aligned} \Delta u(\mathbf{x}) + k^2(b(\mathbf{x}) + 1)u(\mathbf{x}) = 0 \quad \text{in} \quad \mathbb{R}^2 \\ u(\mathbf{x}) = \mathrm{e}^{ik\mathbf{x}\cdot d} + u^s(\mathbf{x}) \\ \lim_{r\to\infty} r\left(\frac{\partial u^s(\mathbf{x})}{\partial r} - iku^s(\mathbf{x})\right) = 0 \end{aligned} \tag{2.1}$$

where $u^s(\mathbf{x})$ is the scattered field, $r = |\mathbf{x}|$, k is the wave number [23].

For the intend of this thesis, the refractive index is assumed to be constant on D,

$$b(\mathbf{x}) = \begin{cases} \mathbf{b}, & \text{if } \mathbf{x} \in D \\ \\ 0, & \text{if } \mathbf{x} \in \mathbb{R}^2 - D \end{cases}$$

for $\mathbf{b} \neq -1 \in \mathbb{R}$.

The Sommerfeld radiation condition (the third line of the equation (2.1)) guarantees that the scattered wave is outgoing and decaying. The existence and uniqueness of solutions for the equation (2.1) is assured [23]. Hence, the direct problem is well posed.

Current methods for modeling time-harmonic waves through inhomogeneities applying finite difference or finite element techniques to the Helmholtz differential equation lead to sparse, Hermitian matrices that show increasingly poor conditioning as the discretization is refined. An alternative to a finite element or finite difference discretization is to formulate the Helmholtz equation as the Lippmann-Schwinger equation. The numerical solution of this equation only requires discretization of the scattering domain and satisfies the outgoing condition automatically.

2.1.2 The Lippmann-Schwinger Equation

The scattering problem (2.1) is equivalent to the Lippmann-Schwinger equation (for further details see [23]), which is a weakly singular integral equation given by

$$u(x) = u^i - k^2 \int_D \Phi(k|x-y|)b(y)u(y)dy \tag{2.2}$$

where

$$\Phi(r) = -\frac{i}{4} H_0^{(1)}(r) \tag{2.3}$$

and $H_0^{(1)}$ is the Hankel function of the first class of order zero.

The equation (2.2) is more compactly expressed as

$$\mathbf{A} = \mathbf{I} + \mathbf{K} \tag{2.4}$$

where $\mathbf{A} : L^2(\mathbb{R}^2) \longrightarrow L^2(\mathbb{R}^2)$ is continuously invertible on the Hilbert space $L^2(\mathbb{R}^2)$, $\mathbf{I}$ is the identity operator, and $\mathbf{K}$ is the integral operator given by

$$(\mathbf{K}u)(x) = k^2 \int_D \Phi(k|x-y|)b(y)u(y)dy. \tag{2.5}$$

Note that the integral operator $\mathbf{K}$ is a convolution operator with a weakly singular kernel. Thus, the operator $\mathbf{K}$ on the Hilbert space $L^2(\mathbb{R}^2)$ is a compact operator, and therefore bounded [23].

The numerical solution of (2.2) requires efficient and high-order quadrature rules. In this thesis, we introduce a numerical solution based on the discretization of Vainikko [85] and a corrected trapezoidal rule [2].

2.1.3 Discretization of Vainikko

Vainikko [85] introduces an approach for piecewise smooth (discontinuous) scatterers that produces $O(h^2(1 + \log h))$ convergence, where h is the discretization spacing in each direction. This approach requires approximating the area fraction of each cell that lies on each side of a discontinuity in the refractive index.

To the numerical handling of the integral equation (2.2), it is assumed that the scattered lies inside a square domain $G = [l, L] \times [l, L]$, $D \subset G$ for some l, $L \in \mathbb{R}$, $L > l$, and it is taken $h = (L - l)/N$ for some $N \in \mathbb{N}$.

For every $j = (j_1, j_2) \in \mathbb{Z}^2$, let $x_{j,h} = (l, l) + jh$ and $B_{j,h}$ the square of area

h^2 centered at the point $x_{j,h}$, i. e.,

$$B_{j,h} = \left\{ x = (x_1, x_2) \in \mathbb{R}^2 : l + \left(j_k - \frac{1}{2} \right) h < x_k < l + \left(j_k + \frac{1}{2} \right) h, \ \ k = 1, 2 \right\}.$$

The grid approximation of b is defined as follows

$$b_{j,h} = \begin{cases} b(x_{j,h}), & \text{if} \quad B_{j,h} \cap \partial D = \emptyset \\ \\ b(x_{j,h}) \text{meas}(B_{j,h}^{(p)}) h^{-2}, & \text{if} \quad B_{j,h} \cap \partial D \neq \emptyset \end{cases}$$

where $B_{j,h}^{(p)}$ is the connectivity component of the open set $B_{j,h} \setminus \partial D$ wich contains $x_{j,h}$.

Let us define

$$\Phi_{j,h} = \begin{cases} \Phi(k|j|h), & \text{if} \quad j \neq 0 \\ \\ 0, & \text{if} \quad j = 0. \end{cases}$$

We denote with $G_{N,h}$ the grid points

$$G_{N,h} = \{ x_{j,h} : j \in \mathbb{Z}_N^2 \} \tag{2.6}$$

where $\mathbb{Z}_N^2 = \{ j \in \mathbb{Z}^2 : 0 \leq j_k \leq N, k = 1, 2 \}$,

the equation (2.2) is approximated by the discrete equation

$$u_{j,h} = u_{j,h}^i - h^2 k^2 \sum_{l \in \mathbb{Z}_N^2} \Phi_{j-l,h} b_{l,h} u_{l,h} \quad (j \in \mathbb{Z}_N^2). \tag{2.7}$$

The equation (2.7) in matrix form is

$$(K + I) u_h = u_h^i. \tag{2.8}$$

The system (2.8) is uniquely solvable for all sufficiently small $h > 0$ and

$$\max_{j\in\mathbb{Z}_N^2} |u_{j,h} - u(jh)| \leq ch^2(1 + |\ln h|). \tag{2.9}$$

For details see Theorem 2.1 in [85]. On the other hand, the operator $\mathbf{A} = \mathbf{I} + \mathbf{K}$ is a compact perturbation of the identity. The compactness of $\mathbf{K}$ implies that there exist only a finite number of eigenvalues of $\mathbf{K}$ outside any ball of nonzero radius around the origin [53]. For compact perturbations of the identity, Generalized Minimum Residual Method (GMRES) converges superlinearly at a rate determined by the distribution of the eigenvalues [86]. On account of this, we solve the discrete system (2.8) using GMRES implementation of the **Scipy** library.

2.1.4 Corrected Trapezoidal Quadrature Rule

A fourth order corrected trapezoidal rule is applied to deal with the logarithmic singularity of the integral operator (2.5) using the correction coefficients calculated in [2].

$$u_{j,h} = u^i_{j,h} - h^2k^2 \sum_{l\in\mathbb{Z}_N^2} \Phi_{j-l,h} b_{l,h} u_{l,h} \quad + O(h^4), \;\; j \in \mathbb{Z}_N^2 \tag{2.10}$$

where

$$\Phi_{j,h} = \begin{cases} \Phi(k|j|h), & \text{if} \quad j \neq 0 \\ \Phi_{j,h} = \beta_1, & \text{if} \quad j = 0, \end{cases}$$

$\beta_1 = -\frac{i}{4} + \frac{1}{2\pi}\left(\ln\left(\frac{hk}{2}\right) + \gamma + c_1\right)$ and c_1 is a corrected coefficient (see details in [2]).

The equation (2.10) in matrix form is

$$(K_T + I)u_h = u^i_h. \tag{2.11}$$

K_T is an $n \times n$ matrix , $n = (N+1)^2$.

A way to solve (2.11) efficiently is using the structure of the arising matrix

K_T, Figure 2.2.

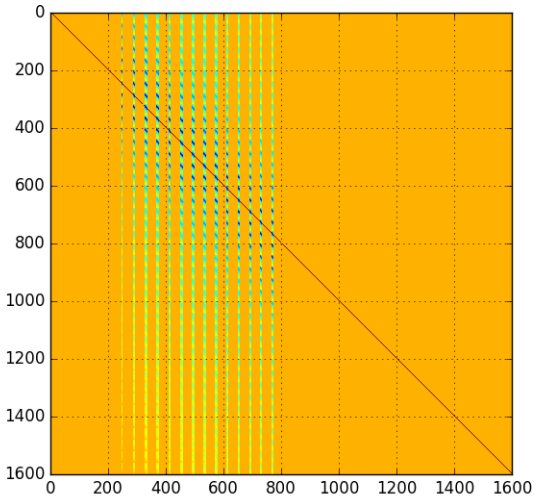

Figure 2.2: Drawing values of K_T obtained in example 2.1.1.

Let us denote the sets of indices by

$$\begin{aligned} i_{in} &= \{j : b(jh) \neq 0\} \\ i_{out} &= i_{in}^c. \end{aligned}$$

The columns and rows of the matrix $K_T + I$ are reordered in this way; first, the columns and rows with index in the set i_{out}. Thus, $K_T + I$ becomes a matrix in the form

$$\left(\begin{array}{c|c} I & C_{12} \\ \hline 0 & C_{22} \end{array}\right)$$

where C_{12} is a submatrix $n_{out} \times n_{in}$ and C_{22} is $n_{in} \times n_{in}$

$$\begin{aligned} n_{in} &= \#i_{in} \\ n_{out} &= n - n_{in}. \end{aligned}$$

Hence, the system solution is

$$u_h^r = \left(\frac{u_1}{u_2,} \right)$$

$$\begin{aligned} u_2 &= C_{22}^{-1} u_2^i \\ u_1 &= u_1^i - C_{12} u_2. \end{aligned}$$

u_1^i and u_2^i are the vectors corresponding to the reordering of the vector u_h^i. The numerical solution u^h is obtained permuting the elements of u_h^r. This reordering of $K_T + I$ decreases the computational time to solve (2.11); it is solved $C_{22} u_2 = u_2^i$ and a matrix-vector product.

The numerical solver of the direct scattering problem using either, Vainikko or Trapezoidal method is denoted by F,

$$u_h = F(D, b) \tag{2.12}$$

F is known as the *forward mapping*.

2.1.5 Numerical Example

In this section, a numerical example is given to show the effectiveness of the discrete solution of the Lippmann-Schwinger equation discussed in section 2.1.4. The method of Vainikko is used to compare computational times.

Example 2.1.1 *We shall consider the kite (introduced in [51]) with refractive index* $\mathbf{b} = 25$ *depicted in Figure 2.3 (a) as the scattering obstacle. On the other hand, Figure 2.3 (b) shows the real part of the incident field with* $k = 1$, $d = (1, 0)$.

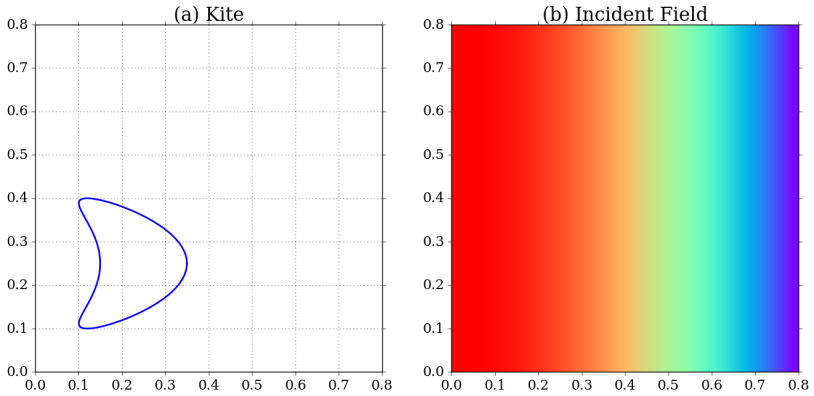

Figure 2.3: (a) Kite described by the equation $x(t) = (1.5\sin(t), \cos(t) + 0.65\cos(2t) - 0.65), 0 \leq t \leq 2\pi$ (b) Real part of the plane wave $\exp(ikd \cdot r)$ with $k = 1$, $d = (1, 0)$.

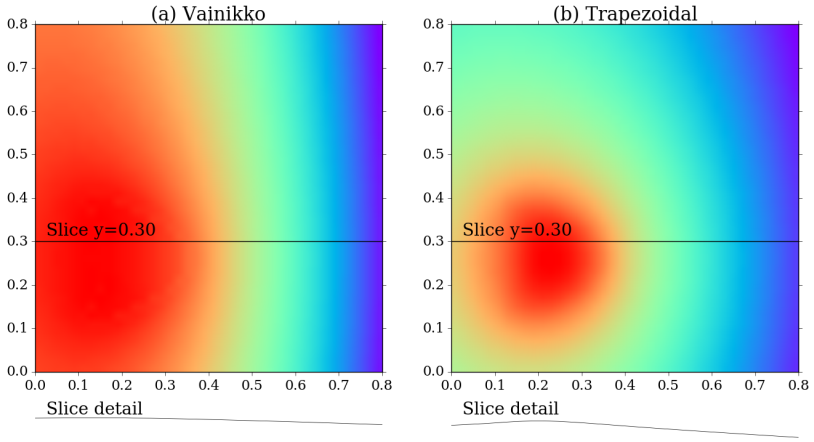

Figure 2.4: (a)-(b) Real part of the scattered field, $\Re(u^s)$.

In Figure 2.4, parts (a) and (b) respectively, the numerical solution using Vainikko and Trapezoidal method are displayed. The incident wave impinges on the obstacle at 0 degree angle with the positive x-axis in both cases.

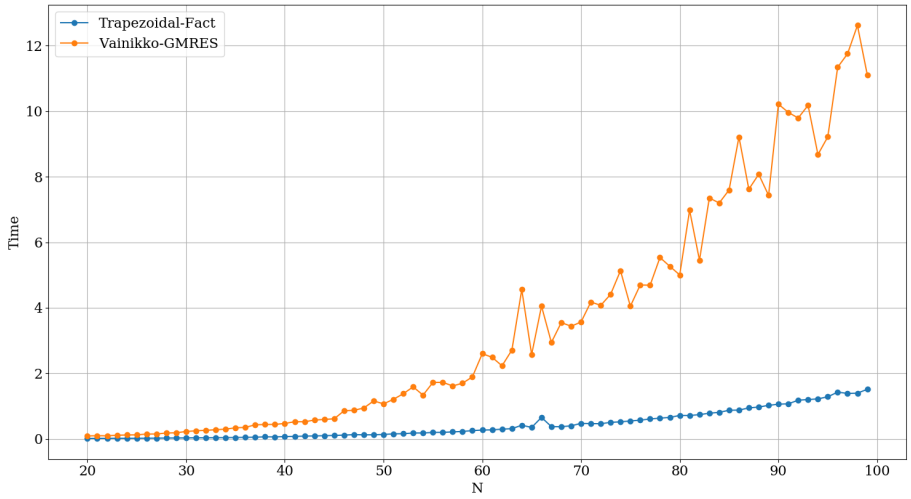

Figure 2.5: Comparison of computational times (in seconds) for solving the Lippmann-Schwinger equation with the configuration depicted in Figure 2.3

From Figure 2.3, it is apparent that the method for the numerical solution of the Lippmann-Schwinger equation introduced in section 2.1.4 is considerably faster than the method of Vainikko.

2.2 High-Level Representation

In this section, it is introduced a parametric representation of the scattering obstacle based on a point cloud, which is a high-level representation. The representation of geometric shapes based on a point cloud is a mature area of computational geometry and has been used for shape and appearance modeling [68, 49, 87]. It has a structural simplicity which supports efficient adaptation. Furthermore, this representation allows us to model prior knowledge of the obstacle in a precise way, i.e. we model into the prior distribution star-shaped scatterers.

Two ways to obtain a smooth boundary of the obstacle D from a point cloud are proposed; one using the convex hull for convex obstacle and another

using the α-shape for a star-shaped obstacle. Of note, through this thesis we have assumed D to be a star-shaped obstacle.

2.2.1 Parametric Representation: Convex Obstacles

Let us $Q = \{p_i\}_{t=1}^{m}$ a set of m points within the domain of the problem, $Q \subset G$. We construct a smooth and convex boundary Γ_Q from *point cloud* Q as follows:

1. Calculate the convex hull of Q, represented by a subset of points $H(Q) \subset Q$. Joining these points creates a convex polygon containing all Q.

2. Compute continuous, smooth, and closed curve Γ_Q interpolating the points that define the polygon $H(Q)$ with a third order B-spline (see Figure 2.6).

This algorithm creates a well defined mapping of Q to a convex boundary Γ_Q.

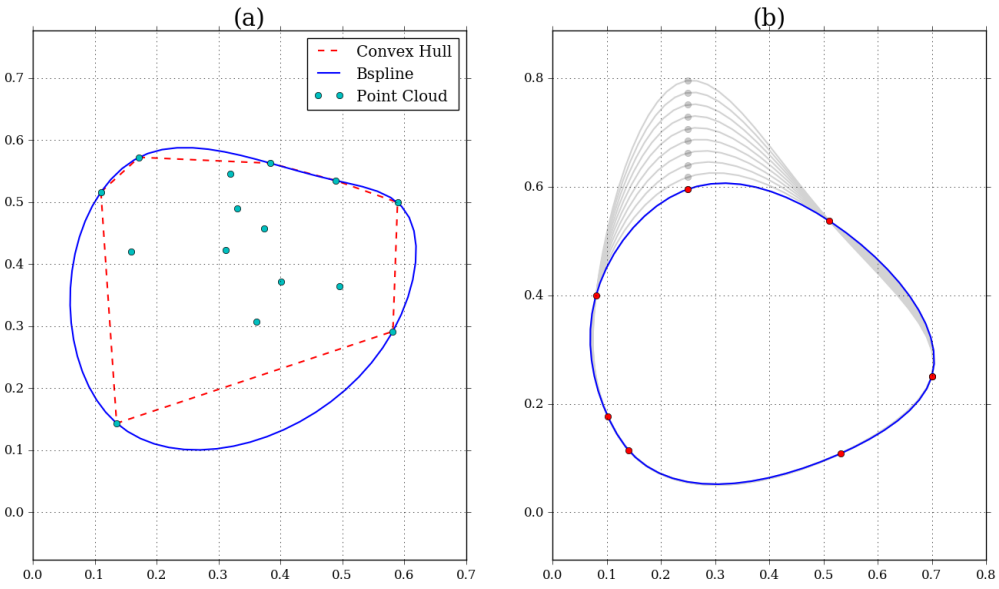

Figure 2.6: (a) The convex hull from a point cloud and the B-spline curve of degree 3 in the points that define the polygon $H(Q)$ (b) When a point of the convex hull is moved. It can be seen the stability of the representation locally.

The significant advantage of spline representations (as opposed to polynomial and series representations) is their local nature [71]. For example, if part of a contour is perturbed by an intrusion the change in a spline representation will affect very few arcs (see Figure 2.6(b)).

2.2.2 Parametric Representation: Star-Shaped Obstacles

In order to consider the case of nonconvex scatterers we shall work with domains D whose boundary is star-shaped, i.e., there is a point $x_0 \in D$ such that every ray that departs from x_0 crosses the boundary ∂D once. This class of nonconvex scatterers is commonly regarded as a benchmark in the literature of inverse scattering problems [23, 15].

To represent a star-shaped obstacle from a *point cloud* Q, the α-shape of Q is calculated. The α-shape of a point cloud is a subgraph of the Delaunay triangulation [31] of the point cloud; two points are connected if there is an empty disk of radius α touching two points. When $\alpha \to \infty$ the disk of radius α is replaced by half-plane, and hence the α-shape of points will be equal to the convex hull of these points. On the other hand, the α-shape of S degenerates to the point-set S when $\alpha \to 0$. This definition is a generalization of the convex hull of a point set and formalize the intuitive notion of its "shape."

The parametric representation of a star-shaped obstacle from a *point cloud* and an α-parameter is introduced in [64]. This parametrization to represent ∂D using the α-shape algorithm [31] is computed as follows;

Algorithm 1: Compute a smooth boundary, $\Gamma_{Q,\alpha}$

Data: $Q = \{p_i\}_{i=1}^{m}$ uniformly distributed on G, α

Step 1. Compute the Delaunay triangulation $DT(Q)$, (Figure 2.8(a))

Step 2. Compute S_α by inspecting all triangles Δ_T in $DT(Q)$:
if *its circumcircle has smaller radius* (r_i) *than* α **then**
accept Δ_T, (Figure 2.8(b)-(c))

Step 3. Get ∂S_α consists of all 1- simplices (the edges of the triangles in S_α) in S_α, which are $\alpha - exposed$, (Figure 2.8(c)(d) and Figure 2.7)

Step 4. Obtain the respective polygon $P(\partial S_\alpha)$, (fig. 2.8(d))

Step 5. Calculate a smooth boundary $\Gamma_{Q,\alpha}$ interpolating the points that define the polygon $P(\partial S_\alpha)$ with a third-order B-spline, (Figure 2.8(d))

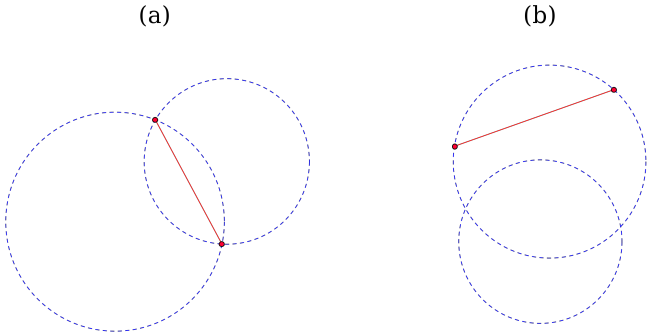

Figure 2.7: (a) not α-exposed (b) α-exposed.

Of note, algorithm 1 creates a well defined mapping from Q and an α-parameter to a boundary $\Gamma_{Q,\alpha}$. Indeed, the polygon $P(\partial S_\alpha)$, and thus the

smooth boundary $\Gamma_{Q,\alpha}$, depends on all cloud points.

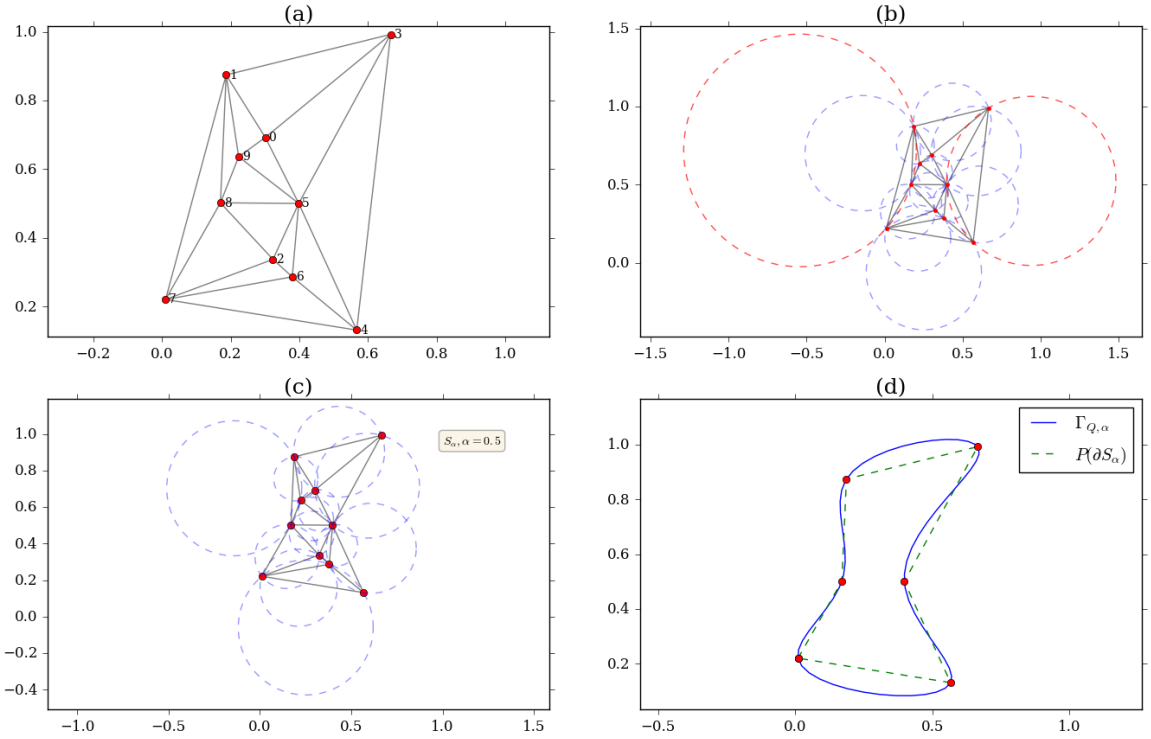

Figure 2.8: (a) Delaunay triangulation, $DT(Q)$ (b) The circumcircles of the Delaunay triangulation (c) S_α; the $\alpha-$ shape from Q with $\alpha = 0.5$ (d) $\Gamma_{Q,\alpha}$; the B-spline curve of degree 3 in the points that define the polygon $P(S_\alpha)$.

It can be said that the α-parameter measures "the non-convexity" of the obstacle. In Figure 2.9, we show how given a cloud of points the parameter α defines the shape of the boundary.

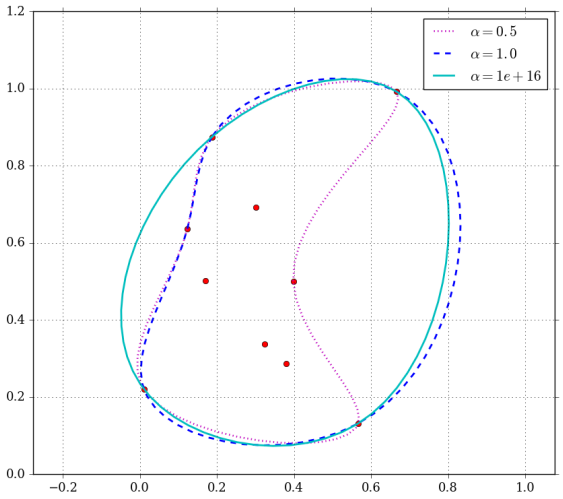

Figure 2.9: $\Gamma_{Q,\alpha}$ for different values of the α.

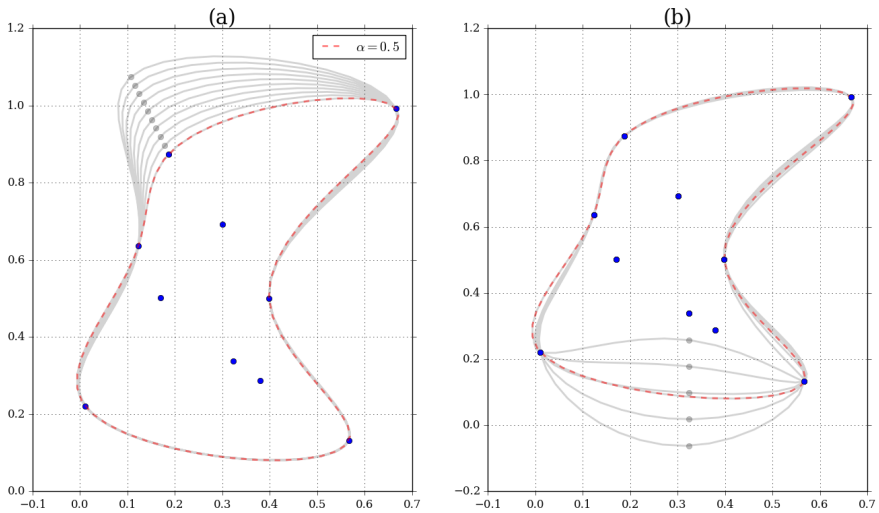

Figure 2.10: (a) $\Gamma_{Q,\alpha}$ with $\alpha = 0.5$, when a point of the ∂S_α is perturbed, (b) and an interior point of S_α is perturbed. It can be perceived the stability of the representation locally.

The parametric representation $\Gamma_{Q,\alpha}$ is locally stable in its interior points and

boundary. Indeed, it can be observed in Figure 2.10 the effect on the boundary $\Gamma_{Q,\alpha}$ when moving a boundary point, and unlike in the convex case, local changes in the interior points cause local changes in the boundary $\Gamma_{Q,\alpha}$.

2.3 Inverse Problem: Bayesian Framework

In this chapter, the inverse scattering problem is formulated in the Bayesian framework. This formulation allows us restating the inverse problem as a well-posed extension in a larger space of probability distributions [48]. The solution of the inverse problem is the posterior probability distribution. The case of recovering a convex obstacle is treated first. Subsequently, the formulation is extended to a star-shaped obstacle using an additional parameter.

2.3.1 Inverse Problem

The inverse scattering problem is defined as follows: given the scattered field u^s on some points of the domain G, estimate the shape of the scatterer D and the refractive index $\mathbf{b}$. The scattered field is obtained from several incoming plane waves with different directions d. This problem is formulated in a finite dimensional space using the parametric representation of the obstacle described in section 2.2. Thereby, the parameter space to be estimated is $\theta = (\theta_g, \mathbf{b})$;

- $\theta_g = Q$ for convex obstacles, and $\theta_g = (Q, \alpha)$ for star-shaped obstacles.
- $\mathbf{b}$ is the refractive index (e.g. in medical applications, it is related to the elastic properties of tissue), it is taken constant on the obstacle.

We refer to θ_g as geometric parameters, and $\mathbf{b}$ as the constitutive parameter. The forward mapping on θ is defined as follows:

$$F_\Gamma(\theta) := F(\Gamma_{\theta_g}, \mathbf{b}). \tag{2.13}$$

F_Γ is well-defined, sections 2.1 and 2.2.

2.3.2 Bayesian Formulation

In Bayesian parameter estimation, $\theta \in \Theta$ is taken as a random variable and the solution of the inverse problem is summarized in the posterior distribution. It shall be assumed that there are measurements of the scattered field $\tilde{u}$ with additive Gaussian noise at the points on $G_{N,h}$

$$\tilde{u} = F_\Gamma(\theta) + \eta \tag{2.14}$$

where $\eta \sim \mathcal{N}(0, \sigma^2)$. The Bayesian solution to our inverse problem is, by virtue of the Bayes' theorem [48]

$$\pi(\theta|\tilde{u}) = \frac{L(\tilde{u}|\theta)\pi(\theta)}{\pi(\tilde{u})} \tag{2.15}$$

where

- The posterior distribution $\pi(\theta|\tilde{u})$ quantifies our uncertainty regarding θ given data $\tilde{u}$.
- The prior distribution $\pi(\theta)$ encodes the information available on the unknown parameters.
- The likelihood $L(\tilde{u}|\theta)$ describes the relation between the observed data and the unknown parameters. In terms of data noise and the governing equation.
- $\pi(\tilde{u})$ is a normalizing constant.

These distributions are settled below.

Likelihood:

The likelihood is given by the noise distribution (2.14),

$$L(\tilde{u}|\theta) \propto \exp\left(-\frac{1}{2\sigma^2}||\tilde{u} - F_\Gamma(\theta)||^2\right) \tag{2.16}$$

assuming independent measurements.

Prior Distribution

The prior distribution for a *convex obstacle* is modeled as follows:

1. The refractive index ($\mathbf{b}$) and the point cloud Q are taken as independent parameters, therefore $\pi(\theta) = \pi(Q)\pi(\mathbf{b})$.

2. A uniform distribution for Q is imposed, as a default selection. Consequently, the prior probability $\pi(Q)$ is constant on the domain G.

3. The choice of a gamma distribution for $\mathbf{b}$ is motivated by the application of the inverse scattering problem in elasticity imaging methods. The refractive index represents the Young modulus [39]. In this manner, the refractive index is assumed as a positive parameter

$$\mathbf{b} \sim Gamma(\tilde{k}, \tilde{\lambda}). \tag{2.17}$$

Likewise, the prior distribution for a *star-shaped obstacle* is modeled as follows:

1. The refractive index ($\mathbf{b}$), the point cloud Q and α are taken as independent parameters, therefore $\pi(\theta) = \pi(Q)\pi(\mathbf{b})\pi(\alpha)$.

2. The distributions $\pi(Q)$, $\pi(\mathbf{b})$ are chosen in the same way that in the convex obstacle case.

3. Once again it is used a uniform distribution as a default selection for the α-parameter. Thus, the prior probability $\pi(\alpha)$ is constant on the domain G.

The arising posterior distribution does not belong to a known family of distributions. Therefore, we resort to an MCMC simulation algorithm to sample from it. The MCMC algorithm requires the evaluation of the energy function, that is minus log of the non-normalized posterior,

$$Energy(\theta) = E - log\, L(\tilde{u}|\theta) - log\, \pi(\mathbf{b}) \tag{2.18}$$

for any suitably chosen constant E. The terms $\log \pi(Q)$ and $\log \pi(\alpha)$ are not considered in the evaluation of the energy because are constant.

2.4 Markov Chain Monte Carlo Method (MCMC)

In this section, an MCMC method with the affine invariant property, motivated by the *t-walk* [21], is constructed to explore the arising posterior distribution. The t-walk is a sampling method proposed by Christen and Fox [21] to sample from general continuous distributions, and its performance is independent of the distribution scale. This property of the MCMC method is called affine invariance, and it implies that the performance of the MCMC method remains independent regardless of the aspect ratio in highly anisotropic distributions. Later, Goodman and Weare introduced this property in *the emcee hammer* [38].

2.4.1 Metropolis-Hastings (MH)

The MH algorithm simulates samples from a probability distribution by making use of the full joint density function and (independent) proposal distributions for each of the variables of interest. The algorithm 2 provides the details of a generic MH algorithm.

Algorithm 2: Metropolis - Hastings Algorithm

1. Pick the initial value $x_1 \in \mathbb{R}^n$ and set $k = 1$.

2. Draw $y \in \mathbb{R}^n$ from $q(x_k, y)$. Calculate

$$\rho(x_k, y) = \min\left\{1, \frac{\pi(y)q(y, x_k)}{\pi(x)q(x_k, y)}\right\}$$

3. Draw $t \in [0, 1]$ from uniform probability density.

4. **if** $\rho(x_k, y) \geq t$ **then**
   set $x_{k+1} = y$, **else**
   $x_{k+1} = x_k$

5. When $k = K$, stop. **else**
   increase $k \to k + 1$ and go to step 2

Note that samples from the proposal distribution are not accepted automatically as posterior samples. These candidate samples are accepted probabilistically based on an acceptance probability [48]. There are mainly two kinds of proposal distributions, symmetric and asymmetric. A proposal distribution is a symmetric if $q(x|y) = q(y|x)$.

The performance of the Metropolis Hastings method depends very much on the proposal distribution used, $q(x, y)$. A proposal distribution that accepts too many or too few proposals will produce highly autocorrelated chains. There are infinite ways to propose the transition kernel Metropolis-Hastings. Typically a naive transition kernel has many numerical efficiency problems.

Below, we introduce a proposal for $q(x, y)$ with the affine invariance property.

2.4.2 MCMC Design for a Convex Obstacle

The Markov Chain Monte Carlo provides a simple and rich ground for building point cloud move proposals in a Metropolis-Hastings (MH) scheme. The

affine invariant proposals on the point cloud to the scattering problem were defined before [64, 29]. In this work, we work further on the proposal for the α parameter. The affine invariant feature may be seen as the capability of the MCMC in locating the obstacle, independently of its relative position in the domain G and its size.

The moves for the cloud points $Q^{(t)} = \{p_i^{(t)}\}_{i=1}^m$ at iteration t are as follows,

1. **Point move:**
   Move randomly a single point $p_k^{(t)} \in Q^{(t)}$

   $$p_k^{(t+1)} = p_k^{(t)} + u_{-k}$$

   where $u_{-k} \sim U(-\bar{d}_{-k}, \bar{d}_{-k})$, and $\bar{d}_{-k}$ is the mean of the pairwise distances

   $$|p_j^{(t)} - p_l^{(t)}| \ \textit{for} \ j \neq l, \quad p_j^{(t)}, p_l^{(t)} \in Q^{(t)} \setminus \{p_k^{(t)}\}.$$

2. **Translate:**
   Move randomly every point in $Q^{(t)}$

   $$p_i^{(t+1)} = p_i^{(t)} + u, \ \ \textit{for} \ 1 < i < m$$

   where $u \sim U(-\bar{d}, \bar{d})$, and $\bar{d}$ is the mean of the pairwise distances

   $$|p_j^{(t)} - p_l^{(t)}|, \ \ \textit{for} \ j \neq l \ \ , p_j^{(t)}, p_l^{(t)} \in Q^{(t)}.$$

We move the parameter using the prior distribution (2.17) as instrumental

$$\mathbf{b} \sim \pi(\mathbf{b}).$$

The instrumental proposal for the obstacle boundary is symmetric because when computing the pairwise distances without the point $p_k^{(t)}$ in the point move, we produce a symmetric proposal on the MCMC. Similarly, when the translation move is chosen, the entire cloud is moved with the same direction u, and therefore the proposal is also symmetric [64]. A detailed description of

the algorithm is as follows:

Algorithm 3: Point Cloud-MH Random Walk 1

Data:

- $Q^{(0)} = \{p_i^{(0)}\}_{i=1}^m$ uniformly distributed on G
- $\mathbf{b}^{(0)} \sim U(0, M_0)$

Step 1. Take $t = 0$

Step 2. Randomly choose:

1. Move randomly a point $p_k^{(t)} \in Q^{(t)}$

$$p_k^{(t+1)} = p_k^{(t)} + u_{-k}$$

2. Move randomly every point in $Q^{(t)} = \{p_i^{(t)}\}_{i=1}^m$

$$p_i^{(t+1)} = p_i^{(t)} + u$$

3. $\mathbf{b}^{(t)} \sim Gamma(\tilde{k}, \tilde{\lambda})$

Step 3. Compute the energy

$$Energy(Q^{(t)}, \mathbf{b}^{(t)}) = -log\, L(\tilde{u}|Q^{(t)}, \mathbf{b}^{(t)}) - log\, \pi(\mathbf{b}^{(t)}).$$

Step 4. Apply the MH criterion

$$\rho = Energy(Q^{(t-1)}, \mathbf{b}^{(t-1)}) - Energy(Q^{(t)}, \mathbf{b}^{(t)})$$

and accept the proposal with probability $e^{-\rho}$.

Step 5. $t = t + 1$

Step 6. Repeat from Step 2 until $t = t_{max}$

In the example displayed in section 3.1, the probability of choosing each proposal is $\frac{1}{3}$.

2.4.3 MCMC Design for a Star-Shaped Obstacle

In this case, there is an additional parameter, α. The proposals for the point cloud Q and the refractive index $\mathbf{b}$ are the same than the convex case. An affine

invariant proposal for α is constructed from the radius of the circumcircles of the Delaunay triangulation in the iteration t, $DT(Q^{(t)})$. Thus,

$$\alpha^{(t+1)} = \frac{1}{2}\alpha^{(t)} + \frac{1}{2}\mathcal{U}(r_{min}, r_{max}) \tag{2.19}$$

where r_{min}, r_{max} are the minimum and maximum radius of the circumcircles of Delaunay triangulation, respectively. The α value is modeled in $[r_{min}, r_{max}]$, given that for values of $\alpha \geq r_{max}$ is obtained always the convex hull and for $\alpha \leq r_{min}$ the set of points.

The probability density function q is given by

$$q(\alpha^{(t+1)}, \alpha^{(t)}) = \frac{2}{r_{max} - r_{min}}\mathcal{I}_C(\alpha^{(t+1)}), \tag{2.20}$$

where $\mathcal{I}_C$ is the characteristic function of the set $\big(\frac{1}{2}(\alpha^{(t)} + r_{min}), \frac{1}{2}(\alpha^{(t)} + r_{max})\big)$. The quotient $\frac{q(\alpha^{(t+1)}, \alpha^{(t)})}{q(\alpha^{(t)}, \alpha^{(t+1)})}$ is a constant on the support of the distribution (2.20). A detailed description of the algorithm is as follows:

Algorithm 4: Point Cloud MH Random Walk 2.

Data:

- $Q^{(0)} = \{p_i^{(0)}\}_{i=1}^m$ uniformly distributed on G
- $\mathbf{b}^{(0)} \sim U(0, M_0)$, $\alpha = \alpha_0$

Step 1. Take $t = 0$

Step 2. Randomly choose:

1. Move randomly a point $p_k^{(t)} \in Q^{(t)}$

$$p_k^{(t+1)} = p_k^{(t)} + u_{-k}$$

2. Move randomly every point in $Q^{(t)} = \{p_i^{(t)}\}_{i=1}^m$

$$p_i^{(t+1)} = p_i^{(t)} + u$$

3. $\mathbf{b}^{(t)} \sim Gamma(\tilde{k}, \tilde{\lambda})$
4. Move α:
   $\alpha^{(t+1)} = 0.5\alpha^{(t)} + 0.5U(r_{min}, r_{max})$

Step 3. Compute the energy

$$Energy(Q^{(t)}, \alpha^{(t)}, \mathbf{b}^{(t)}) = -log\, L(\tilde{u}|Q^{(t)}, \alpha^{(t)}, \mathbf{b}^{(t)}) - log\, \pi(\mathbf{b}^{(t)}).$$

Step 4. Apply the MH criterion

$$\rho = Energy(Q^{(t-1)}, \alpha^{(t-1)}, \mathbf{b}^{(t-1)}) - Energy(Q^{(t)}, \alpha^{(t)}, \mathbf{b}^{(t)})$$

and accept the proposal with probability $e^{-\rho}$.

Step 5. $t = t + 1$

Step 6. Repeat from Step 2 until $t = t_{max}$

In the examples displayed in section 3.2, the probability of choosing each proposal is given by

$$w = \left[\frac{1}{3}, \frac{1}{3}, \frac{1}{6}, \frac{1}{6}\right].$$

Also, the support of α is defined

$$supp(\alpha) = \{\alpha : P(S_\alpha) \text{ is a valid polygon}, \Gamma_{Q,\alpha} \text{ is a valid boundary}\}$$

- $P(S_\alpha)$ is a valid polygon if $P(S_\alpha)$ is a polygon and $Q \subset P(S_\alpha)$.
- $\Gamma_{Q,\alpha}$ is a valid boundary if $\Gamma_{Q,\alpha}$ does not intersect itself and it does not have a peak thinner than the mesh size.

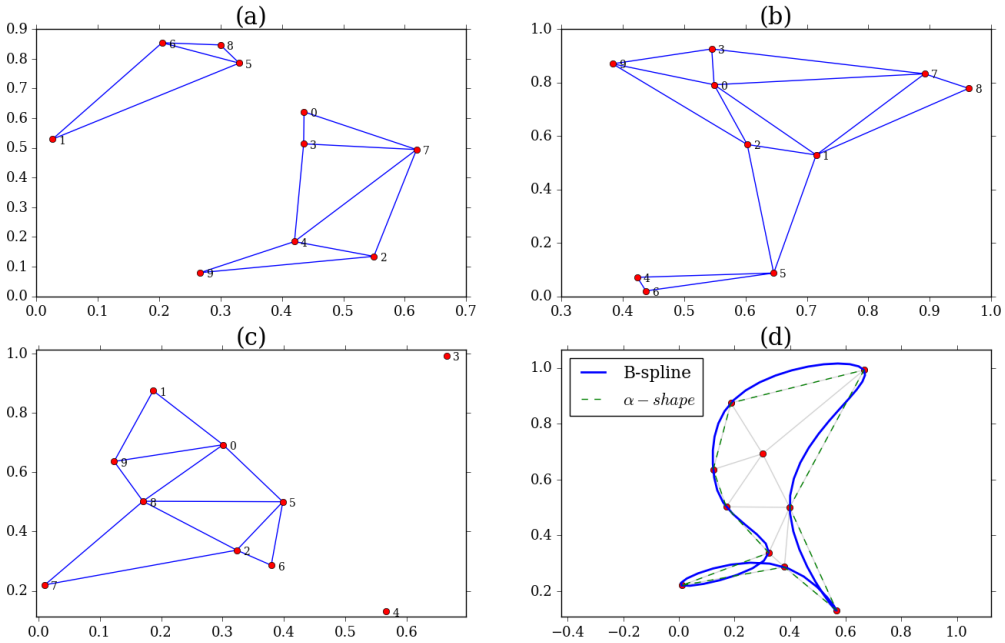

Figure 2.11: (a)-(c) Non-valid S_α (d) non-valid $\Gamma_{Q,\alpha}$.

The Metropolis-Hastings algorithm 4 guarantees that the transition kernel P is irreducible, aperiodic and the measure μ induced by the posterior distribution is asymptotically invariant under P, i.e., μ is a limit distribution for the transition kernel P [48].

This convergence result establishes that the Markov Chain converges asymtotically to a stationary distribution, which is the solution of the inverse problem.

Chapter 3

Results

In this chapter, we offer numerical examples to illustrate the reaches and limitations of our approach to the inverse scattering problem. In section 3.1, the obstacle is assumed to be convex, and the scheme described in section 2.4.2 is used. In section 3.2, a star-shaped obstacle is assumed and the effect of the α parameter to recover the non-convexity of the obstacle using the scheme proposed in section 2.4.3 is shown.

3.1 Numerical Results: Convex Obstacle

In this section is exhibited the results of the reconstruction of an ellipse given by

$$x(t) = (0.3\cos(t), 0.05\sin(t)), \;\; t \in [0, 2\pi] \tag{3.1}$$

with a refractive index, $\mathbf{b} = 25$.

3.1.1 Generation of Synthetic Data

The data has been produced by numerically solving the direct scattering problem in each direction d_i; using the method of Vainikko (as it is described in section 2.1.3) and adding Gaussian noise with mean zero and standard deviation $\sigma = 0.012$. The standard deviation of the noise is computed using the signal to

noise ratio (SNR), defined as:

$$SNR = \frac{magnitude\ of\ signal}{variance\ of\ noise}$$

it is taken the 1% of the magnitude of data.

- Eight incident waves are taken with directions uniformly distributed over the unit circle

$$d_i = \left(\cos\left(\frac{2\pi}{8}i\right), \sin\left(\frac{2\pi}{8}i\right)\right), \quad i = 1, ..., 8.$$

- The search domain we have considered is $G = [-0.5, 0.5] \times [-0.5, 0.5]$.
- We have let $N = 40$ and $h = 0.025$.
- A prior information that obstacle (3.1) is within in G is assumed.
- We let $k = 1$.

3.1.2 Bayesian Parameters

- The instrumental parameters in the prior distribution $\pi(\mathbf{b})$ of the refractive index are taken $\tilde{\lambda} = 1.5$, $\tilde{k} = 60$ which are the scale and shape parameters of the Gamma distribution. i.e. $\mathbb{E}(\mathbf{b}) = \tilde{\lambda}\tilde{k} = 90$ and $\text{var}(\mathbf{b}) = \tilde{\lambda}\tilde{k}^2 = 5400$. The instrumental parameters $\tilde{\lambda}$ and $\tilde{k}$ are chosen of the prior distribution of the refractive index to represent that little is known regarding such parameter, other than it is positive and bounded.
- 200,000 MCMC iterations are performed (computation time: 32.3 hours using Intel Core i5 dual-core 2.5 Ghz processor).
- In [65] we observe that the effective dimension of the parameters space informed by the data is 11. Therefore $m = 10$ points in the point cloud are taken (10 points plus the α parameter).
- The forward map in the likelihood (2.16) is evaluated with the corrected trapezoidal quadrature rule (see section 2.1.4).

3.1.3 Results

Example 3.1.1 *The ellipse defined by the equation (3.1) is reconstructed using the formulation proposed in section 2.4.2.*

The algorithm 3 is implemented in Python. After a burn-in period of 3,000 iterations the chain seems to be sampling from the equilibrium distribution (i.e., the posterior distribution), see Figure 3.1(a).

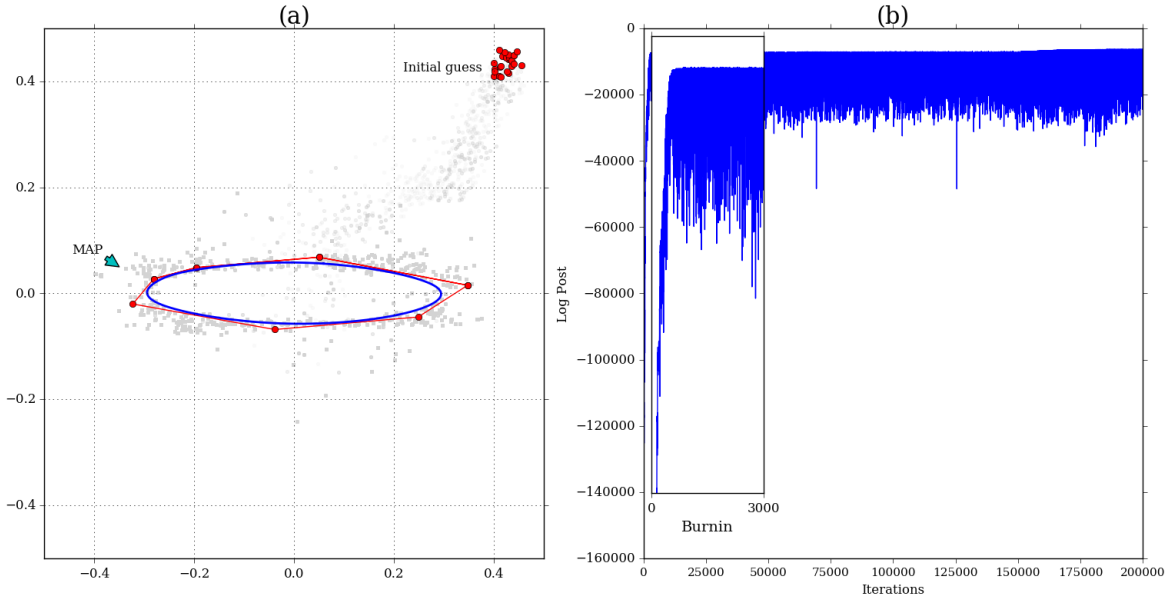

Figure 3.1: (a) After the initial burn-in, the affine invariant point cloud MCMC reaches the region where the scatterer lies. Of note sampling starts in a relatively distant point cloud. (b) Logarithm of the posterior distribution with a burn-in period of 3,000 iterations, after that the MCMC seems to be stable (inset).

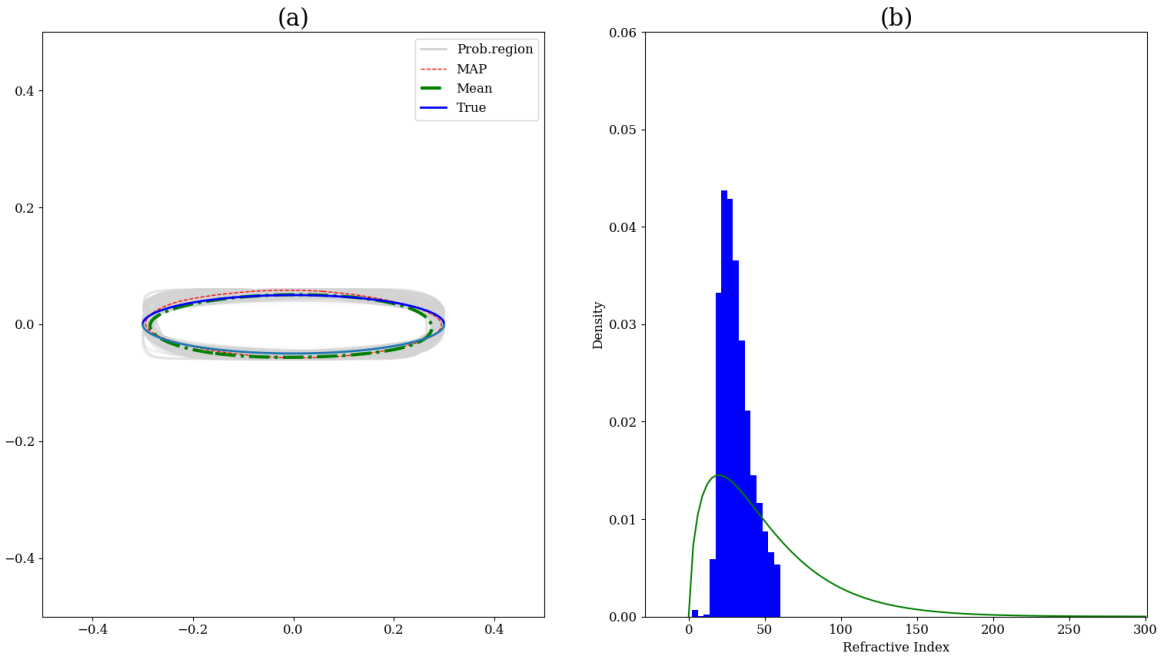

Figure 3.2: After the initial burn-in (3,000 iterations), (a) the true obstacle shown in blue, the maximum a posteriori (MAP) in red, the conditional mean (CM) in green and the probability region obtained through affine invariant MCMC sampling in grey. (b) Prior and marginal posterior distribution for the refractive index $\mathbf{b} = 25$.

In Figure 3.2 trace plots for the conditional mean (CM), the maximum a posterior (MAP) estimator and probability regions are reported. Probability regions are obtained by plotting MCMC simulations after the burn-in period Figure 3.1(a).

The performance of the affine invariant property of MCMC may be seen in Figure 3.1(a), as the cloud of initial points, starting in a small area move and increases in size until the obstacle is found. Moreover, in Figure 3.3 trace plots of the proposals actually accepted, for the three proposals are presented. Note from Figure 3.3(a) how, in a transient period for the first 200 iterations, the translate proposal dominates the accepted moves. This is needed to first

locate the obstacle. The point move is subsequently used, to adapt the obstacle boundary and only then the refractive index is updated. After that, the proposals are accepted at stationary rates as seen in Figure 3.3(b), to explore the posterior distribution (uncertainty) for the scatterer. Note that at this point the translate proposal is seldom used. Of note, a standard MH MCMC is used. The adaptation just described was not decided or set by us, nor 'learned' from the chain itself, since the proposals are selected with probability 1/3 from the onset. Instead, the affine invariant design leads automatically to this transient and stationary adjusting.

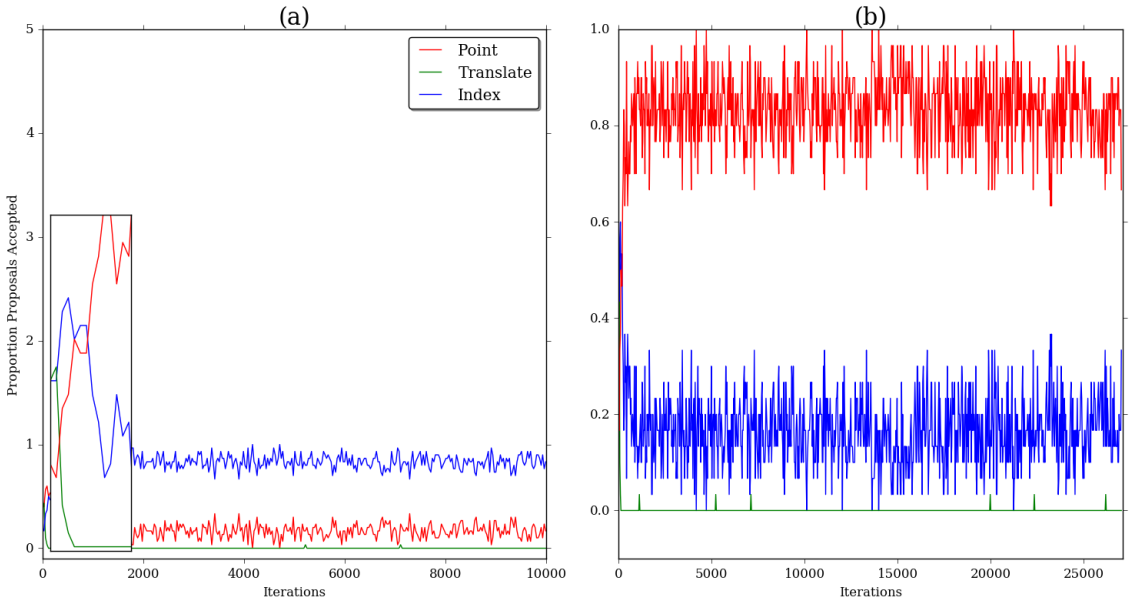

Figure 3.3: (a) Proportion of accepted proposals, every 30 iterations. The translation proposal is first used, to locate the object, then the points are moved to adapt the boundary and finally the refractive index is updated. (b) After the latter transient period, the proposals are accepted at stationary rates. Note, however, that from the onset the proposals are selected with probability 1/3 and that we are working with a standard homogeneous Metropolis-Hastings Markov Chain Monte Carlo: adaptation is a result of the affine invariant design of the transition kernel.

By construction, it is expected that the chains eventually converge to the

stationary distribution, which also is the posterior distribution. However, we need to know if the chain has converged after M draws. Therefore we will show the results of some criteria that help us to establish the convergence of the chain.

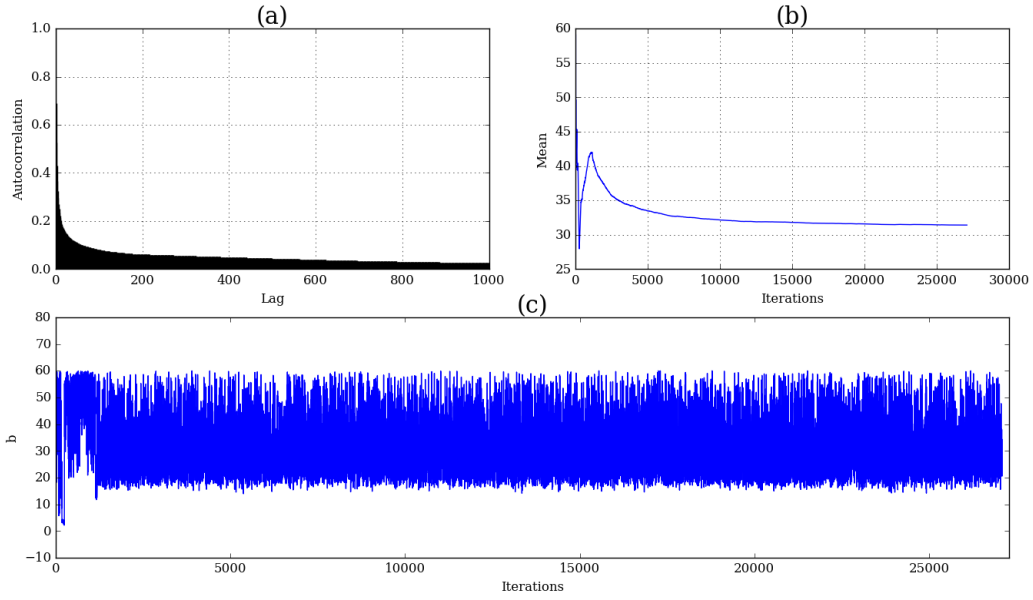

Figure 3.4: (a) Autocorrelation (b) iterations against the mean of the draws up to each iteration (c) Iteration number against the value of the index refractive draw at each iteration.

- One way to see if our chain has converged is to see how well our chain is mixing or moving around the parameter space, which is shown in the Figure 3.4(a)(b).
- Correlations between draws of the Markov chain are evaluated. One should expect a smaller autocorrelation lag if t increases, Figure 3.4(c).

Finally, making the diagnostic of Gelman Rubin [27], we get a "shrink factor" (R) $R = 1.0819746481999699$, which tells us that all chains have escaped from their starting points influence and have traversed all of the target distribution.

Then, with this diagnosis, and considering the points from above, it can be ensured that the chain is sampling from the posterior distribution.

3.2 Numerical Results: Star-Shaped Obstacle

In this section, several numerical tests for the reconstruction of the kite are presented. The kite was introduced by Kirsch in [51]. From there, it has been used as a benchmark in the literature of inverse scattering problems. Of note, the kite is a star-shaped obstacle. The boundary of the kite is described by

$$x(t) = (1.5\sin(t), \cos(t) + 0.65\cos(2t) - 0.65), \;\; 0 \leq t \leq 2\pi. \tag{3.2}$$

with refractive index $\mathbf{b} = 25$. This figure is of interest for two reasons: firstly because it is non-convex and secondly, because it possesses detailed structures (the wings) that are small compared with the scale of the figure and hence should be difficult to recover with a fixed frequency in the probing wave.

3.2.1 Generation of Synthetic Data

The data has been produced by numerically solving the direct scattering problem in each direction d_i; using the method of Vainikko (as it is described in section 2.1.3) and adding Gaussian noise with mean zero and standard deviation $\sigma = 0.012$. The standard deviation is taken the same that in the example of the convex case.

- Eight incident waves are taken with directions uniformly distributed over the unit circle

$$d_i = \left(\cos\left(\frac{2\pi}{8}i + \gamma\right), \sin\left(\frac{2\pi}{8}i + \gamma\right)\right), \quad i = 1, ..., 8.$$

  with $\gamma = 0, \; \frac{\pi}{6}$.

- The search domain we have considered is $G = [0, 0.8] \times [0, 0.8]$.

- We have taken $N = 40,\ 80.\ h = 0.02,\ 0.01.$

- A prior information that obstacle (3.2) is within in G is assumed.

- $k = 1, 5$ are taken at alternating incident directions.

3.2.2 Bayesian Parameters

- The instrumental distribution for $\mathbf{b}$ is taken as in the example of the convex case (section 3.1).

- 2,000,000 MCMC iterations are performed (computation time: 22 hours using Intel Core i7-4790K 4.00 Ghz processor), and $m = 10$ points in the point cloud (for the result mentioned above).

- The forward map in the likelihood (2.16) is evaluated with the corrected trapezoidal quadrature rule (see section 2.1.4).

3.2.3 Results

Example 3.2.1 *The kite (3.2) is reconstructed using the formulation proposed in section 2.4.3. In this example* $k = 1$, $N = 40$, $h = 0.02$ *and* $\gamma = 0$.

After a burn-in period of 10,000 iterations the chain seems to be sampling from the equilibrium distribution (i.e. the posterior distribution), see Figure 3.6.

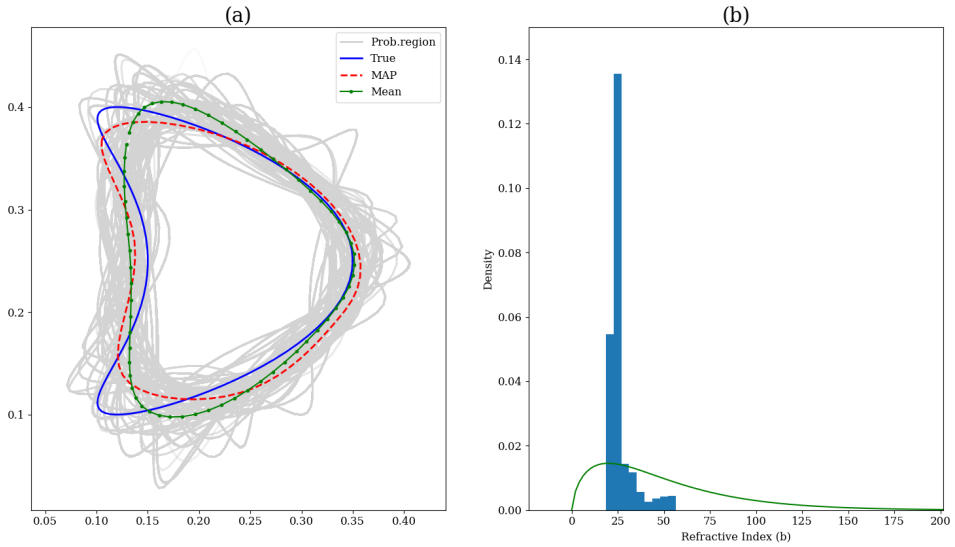

Figure 3.5: After the initial burn-in (10,000 iterations), (a) the true obstacle shown in blue, the maximum a posteriori (MAP) in red, conditional mean (CM) in green and the probability region obtained through affine invariant MCMC sampling in grey (the last 20,000 MCMC iterations). (b) Prior and marginal posterior distribution for the refractive index $\mathbf{b} = 25$.

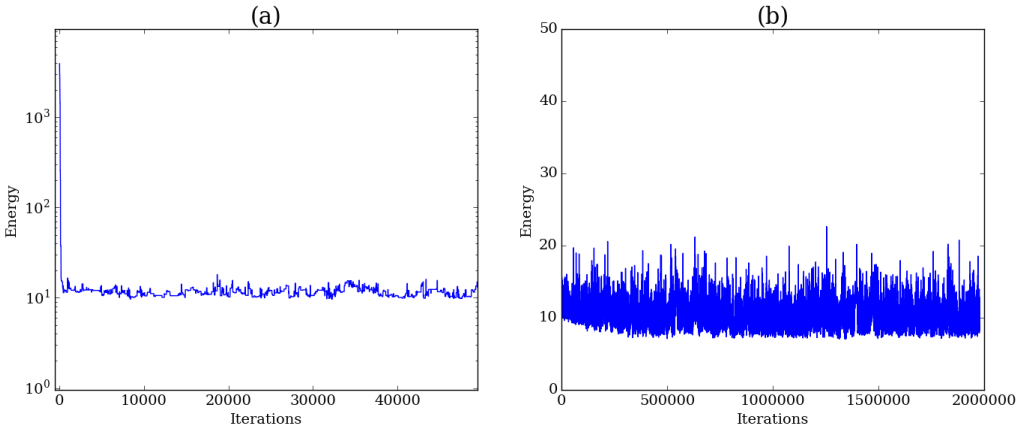

Figure 3.6: Logarithm of the posterior distribution, (a) first 50,000 MCMC iterations (logarithmic scale), (b) and with a burn-in period of 10,000 iterations, after that the MCMC seems to be stable.

In Figure 3.5, trace plots for the maximum a posterior (MAP) estimator, conditional mean (CM) and probability regions are reported. Probability regions are obtained by plotting MCMC simulations after the burn-in period, see burn-in in Figure 3.6 (a).

For a fixed frequency $k = 1$, it is difficult to recover the non-convex part of the kite, Figure 3.5(a). If the wavelength of the incident field is small with respect to the size of the obstacle, there will be a shadow behind the obstacle and the interaction between the wave and obstacle is weaker in this region. To improve the resolution, it is desirable to use an incident field with a shorter wavelength or higher frequency to illuminate the scatterer[9].

In the following example, two frequencies are used for the incident field, $k = 1$ and $k = 5$.

Example 3.2.2 *Two frequencies are taken to recover the kite (3.2)*

- $k = 1$*, in the directions* d_1, d_3, d_5, d_7

- $k = 5$*, in the directions* d_2, d_4, d_6, d_8.

It is taken $N = 40$*,* $h = 0.02$ *and* $\gamma = 0$.

After a burn-in period of 50,000 iterations the chain seems to be sampling from the equilibrium distribution (i.e. the posterior distribution), see Figure 3.7 and Figure 3.8.

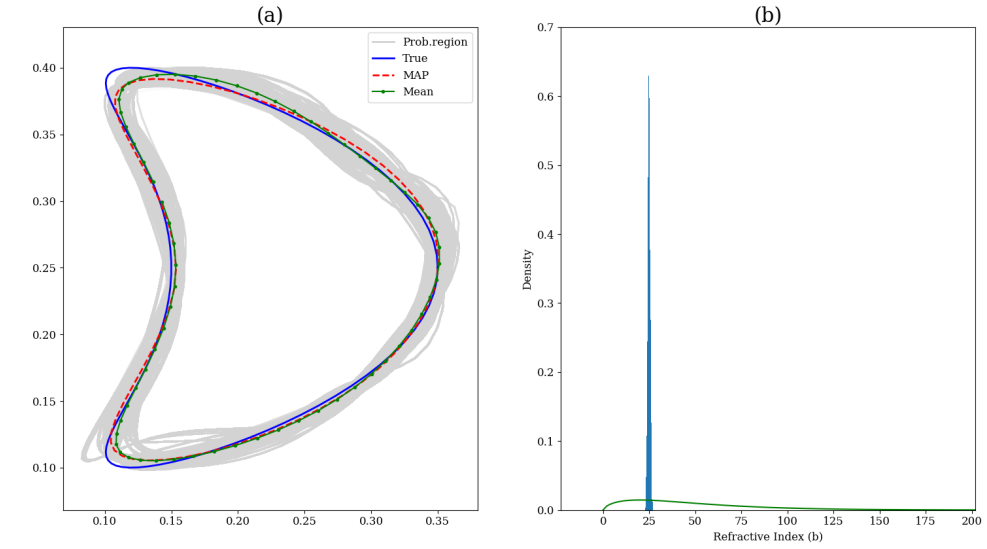

Figure 3.7: After the initial burn-in (50,000 iterations), (a) the true obstacle shown in blue, the maximum a posteriori (MAP) in red, conditional mean (CM) in green and the probability region obtained through affine invariant MCMC sampling in grey (the last 20,000 MCMC iterations). (b) Prior and marginal posterior distribution for the refractive index $\mathbf{b} = 25$.

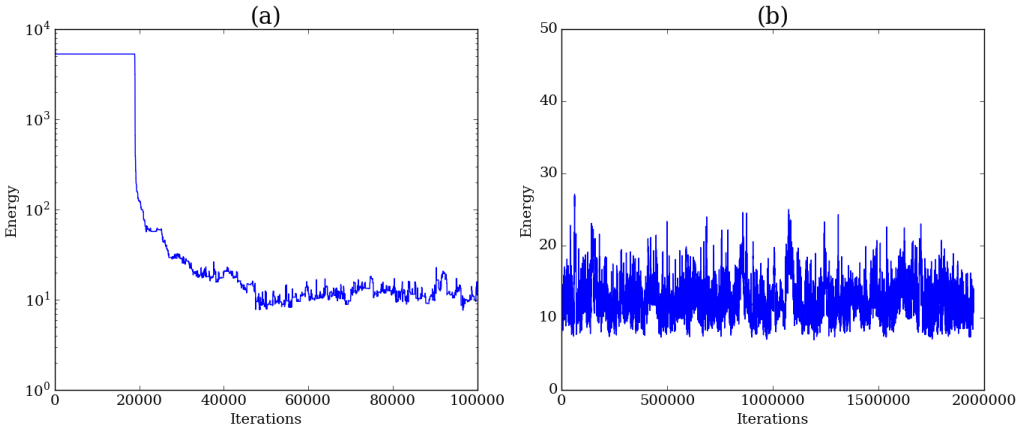

Figure 3.8: Logarithm of the posterior distribution, (a) first 100,000 MCMC iterations (logarithmic scale), (b) and with a burn-in period of 50,000 iterations, after that the MCMC seems to be stable.

In Figure 3.7, the effect of using two scales for the frequency is observed. A higher resolution in the non-convex part of the kite is achieved.

To show that the results obtained are independent of the directions of the incident field, an example in which none of these directions coincide with an axis of symmetry of the obstacle is attempted.

Example 3.2.3 *In this example, we considered the data of example above and the directions in the incident field are rotated taking* $\gamma = \frac{\pi}{6}$.

After a burn-in period of 50,000 iterations the chain seems to be sampling from the equilibrium distribution (i.e. the posterior distribution), see Figure 3.10.

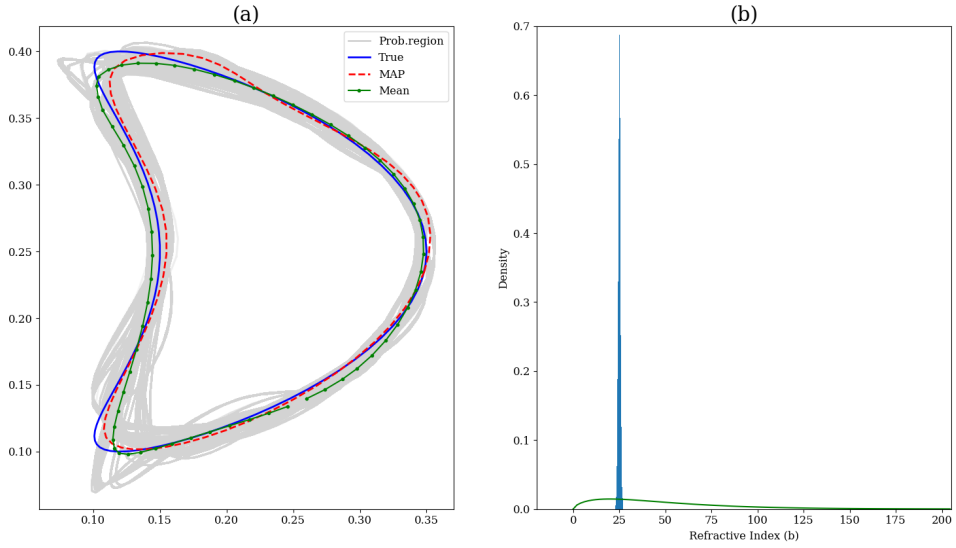

Figure 3.9: After the initial burn-in (50,000 iterations), (a) the true obstacle shown in blue, the maximum a posteriori (MAP) in red, conditional mean (CM) in green and the probability region obtained through affine invariant MCMC sampling in grey (the last 20,000 MCMC iterations). (b) Prior and marginal posterior distribution for the refractive index $\mathbf{b} = 25$.

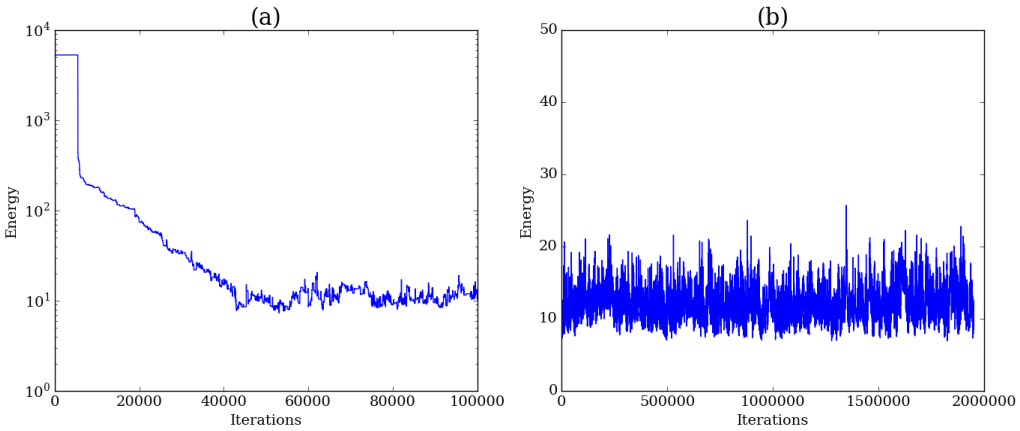

Figure 3.10: Logarithm of the posterior distribution, (a) first 100,000 MCMC iterations (logarithmic scale), (b) and with a burn-in period of 50,000 iterations, after that the MCMC seems to be stable.

The refinement of the mesh is also an important parameter to consider in this approach. In the following example, the effect of a finer mesh on the approach is illustrated.

Example 3.2.4 *In this example, the data is taken from example 3.2.2, and we refined the mesh taking* $N = 80$, $h = 0.01$.

After a burn-in period of 50,000 iterations the chain seems to be sampling from the equilibrium distribution (i.e. the posterior distribution), see Figure 3.12.

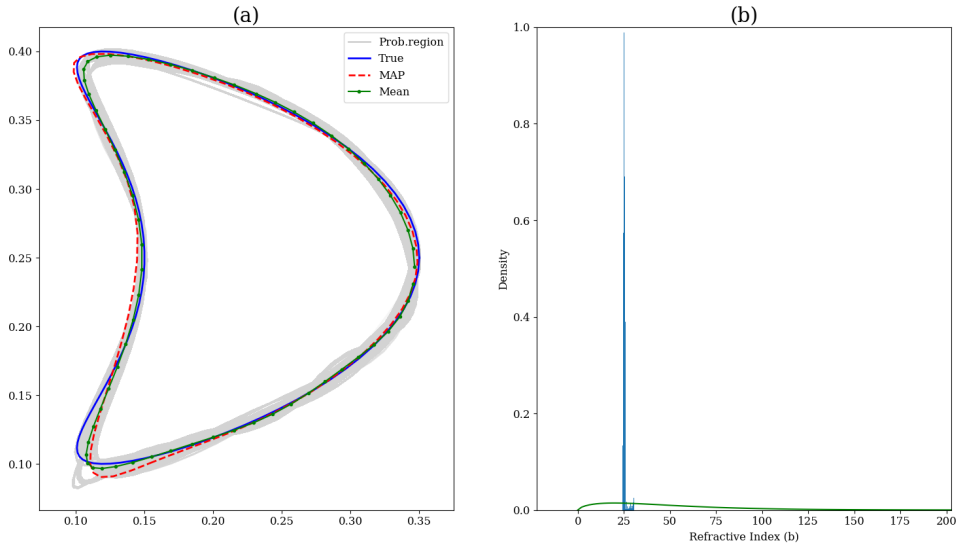

Figure 3.11: After the initial burn-in (50,000 iterations), (a) the true obstacle shown in blue, the maximum a posteriori (MAP) in red, conditional mean (CM) in green and the probability region obtained through affine invariant MCMC sampling in grey (the last 20,000 MCMC iterations). (b) Prior and marginal posterior distribution for the refractive index $\mathbf{b} = 25$.

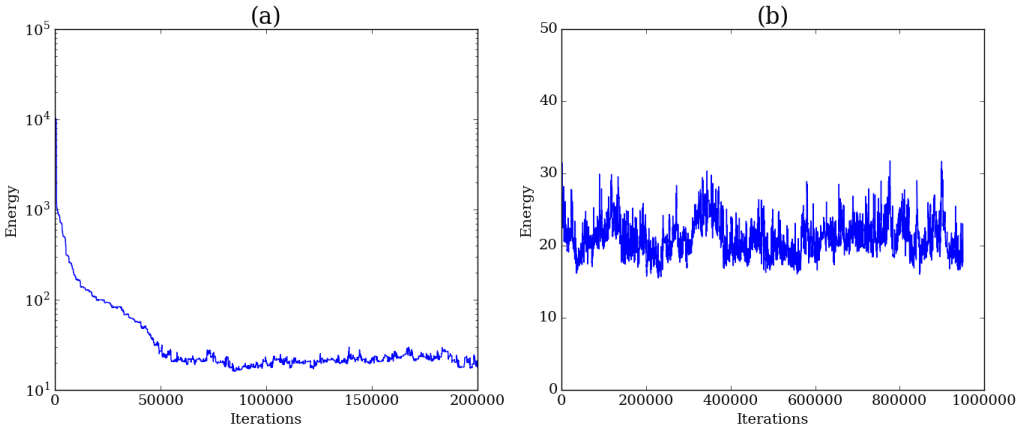

Figure 3.12: Logarithm of the posterior distribution, (a) first 200,000 MCMC iterations (logarithmic scale), (b) and with a burn-in period of 50,000 iterations, after that the MCMC seems to be stable.

In this example, a finer mesh to solve the direct problem has allowed us to recover the kite with higher resolution. Although the number of iterations in which the MCMC converges is reduced Figure 3.12(b), the computational time increases because the evaluation of the forward mapping is more expensive. In this point, we need to make a compromise between the accuracy of the forward mapping and the convergence of the MCMC to the posterior distribution. A result that relates the precision in the solution of the forward mapping and the approach to the posterior distribution has been previously discussed in Capistrán et al. [18].

Chapter 4

Summary and Conclusions

In this thesis, we address a classical inverse scattering problem: to determine the shape of a scattered D and the refractive index $\mathbf{b}$ from the scattered field u^s and the incident field u^i. Of note, this is a challenging problem given that is non-linear and ill-posed. In this thesis we have introduced a method to recover both, the support of the scatterer and the constant refractive index. This method relies on the finite rank property of the direct problem, i.e., the derivative of the direct problem can be arbitrarily approximated by a finite rank operator, giving rise to a low dimensional data-informed subspace.

In this thesis, the following methods are proposed:

1. A efficient numerical solution of the direct scattering problem.
2. A high-level representation based on a point cloud to parameterize the support of the obstacle.
3. The Bayesian formulation of the inverse scattering problem on a low-dimensional space.
4. The design of an affine invariant MCMC that allows us to locate the obstacle regardless of the size, location, and its shape.

In a first approach to the problem, we consider only convex obstacles. This result is reported in Daza et al.[29]. Later, this result is extended to a

star-shaped obstacle using the α-shape algorithm. Below we describe in detail the results obtained in each approach.

The following remarks summarize our findings in the case of convex obstacles:

- the parameter space (location, shape and constitutive properties of the obstacle) is recovered for a fixed frequency, Figure 3.2
- the efficiency of the MCMC affine invariant is showed by adapting to the multiple scales (size, location, and shape) of the problem, Figure 3.3.

In the case of star-shaped obstacles, we had the following findings:

- a parametric representation of star-shaped obstacles calculating the α-shape of a point cloud
- for an incident field with $k = 1$, we did not get good results due to the different size scales that have a non-convex obstacle, Figure 3.5
- to improve the resolution, it is used a low-wavenumber data to locate the scatterer approximately, and higher-wavenumber data to resolve details, Figure 3.7.

The numerical approximation that we have proposed in this thesis to address the scattering problem does not have free parameters. The wavenumbers are comparable with the diameter of the scatterer. The number of points in the point cloud is chosen using the result of the effective dimension obtained in [65].

Note that when the scatterer is a non-convex obstacle, we show that data at a low frequency does not allow us to recover the non-convex part. For the case of star-shaped using two numbers of waves gives us good approximations. We believe that our approach can be generalized to recover arbitrarily-shaped obstacles using multiple frequencies.

Bibliography

[1] J. Aguilar and Y. Chen. A high-order, fast algorithm for scattering calculation in two dimensions. *Computers & Mathematics with Applications*, 47(1):1–11, 2004.

[2] J. C. Aguilar and Y. Chen. High-order corrected trapezoidal quadrature rules for functions with a logarithmic singularity in 2-d. *Computers & Mathematics with Applications*, 44(8):1031–1039, 2002.

[3] H. Ammari, E. Iakovleva, and D. Lesselier. Amusic algorithm for locating small inclusions buried in a half-space from the scattering amplitude at a fixed frequency. *Multiscale Modeling and Simulation*, 3(3):597–628, 2005.

[4] H. Ammari, H. Kang, E. Kim, K. Louati, and M. Vogelius. A music-type algorithm for detecting internal corrosion from electrostatic boundary measurements. *Numerische Mathematik*, 108(4):501–528, 2008.

[5] F. Andersson and A. Holst. A fast, bandlimited solver for scattering problems in inhomogeneous media. *Journal of Fourier Analysis and Applications*, 11(4):471–487, 2005.

[6] I. I. Argatov and F. J. Sabina. Acoustic scattering by a cluster of small sound-soft obstacles. *Wave Motion*, 47(8):537–551, 2010.

[7] S. Asaeedi, F. Didehvar, and A. Mohades. α-concave hull, a generalization of convex hull. *Theoretical Computer Science*, 2017.

[8] M. Banterle, C. Grazian, A. Lee, and C. P. Robert. Accelerating metropolis-hastings algorithms by delayed acceptance. *arXiv preprint arXiv:1503.00996*, 2015.

[9] G. Bao, P. Li, J. Lin, and F. Triki. Inverse scattering problems with multi-frequencies. *Inverse Problems*, 31(9):093001, 2015.

[10] J. Bercoff, M. Tanter, and M. Fink. Supersonic shear imaging: A new technique for soft tissue elasticity mapping. *IEEE Transactions on ultrasonics, ferroelectrics, and frequency control*, 51(4):396–409, 2004.

[11] O. P. Bruno and E. M. Hyde. Higher-order fourier approximation in scattering by two-dimensional, inhomogeneous media. *SIAM Journal on Numerical Analysis*, 42(6):2298–2319, 2005.

[12] O. P. Bruno and A. Sei. A fast high-order solver for problems of scattering by heterogeneous bodies. *IEEE Transactions on Antennas and Propagation*, 51(11):3142–3154, 2003.

[13] J. L. Buchanan, R. P. Gilbert, A. Wirgin, and Y. S. Xu. *Marine Acoustics: Direct and Inverse Problems*. Society for Industrial and Applied Mathematics, 2004.

[14] M. Burger and S. J. Osher. A survey on level set methods for inverse problems and optimal design. *European Journal of Applied Mathematics*, 16(02):263–301, 2005.

[15] F. Cakoni and D. L. Colton. *A qualitative approach to inverse scattering theory*. Springer, 2014.

[16] D. Calvetti. Preconditioned iterative methods for linear discrete ill-posed problems from a bayesian inversion perspective. *Journal of Computational and Applied Mathematics*, 198(2):378–395, 2007.

[17] D. Calvetti and E. Somersalo. Hypermodels in the bayesian imaging framework. *Inverse Problems*, 24(3):034013, 2008.

[18] M. A. Capistrn, J. A. Christen, and S. Donnet. Bayesian analysis of odes: Solver optimal accuracy and bayes factors. *SIAM/ASA Journal on Uncertainty Quantification*, 4(1):829–849, 2016.

[19] M. Cheney. The linear sampling method and the music algorithm. *Inverse Problems*, 17(4):591–595, 2001.

[20] J. A. Christen and C. Fox. A general purpose sampling algorithm for continuous distributions (the t-walk). *Bayesian Analysis*, 5(2):263–281, 2010.

[21] J. A. Christen, C. Fox, et al. A general purpose sampling algorithm for continuous distributions (the t-walk). *Bayesian Analysis*, 5(2):263–281, 2010.

[22] D. Clary and G. Kroes. Scattering and inverse scattering in pure and applied science. *Pike, R*, 2001.

[23] D. Colton and R. Kress. *Inverse acoustic and electromagnetic scattering theory*, volume 93. Springer Science & Business Media, 2012.

[24] D. Colton and P. Monk. A new method for solving the inverse scattering problem for acoustic waves in an inhomogeneous medium. *Inverse Problems*, 5(6):1013, 1989.

[25] D. Colton and P. Monk. A comparison of two methods for solving the inverse scattering problem for acoustic waves in an inhomogeneous medium. *Journal of computational and applied mathematics*, 42(1):5–16, 1992.

[26] S. Cotter, M. Dashti, J. Robinson, and A. Stuart. Bayesian inverse problems for functions and applications to fluid mechanics. *Inverse Problems*, 25:115008, 2009.

[27] M. K. Cowles and B. P. Carlin. Markov chain monte carlo convergence diagnostics: a comparative review. *Journal of the American Statistical Association*, 91(434):883–904, 1996.

[28] M. Dashti and A. M. Stuart. Uncertainty quantification and weak approximation of an elliptic inverse problem. *SIAM Journal on Numerical Analysis*, 49(6):2524–2542, 2011.

[29] M. L. Daza, M. A. Capistrán, J. A. Christen, and L. Guadarrama. Solution of the inverse scattering problem from inhomogeneous media using affine invariant sampling. *Mathematical Methods in the Applied Sciences*, 2016.

[30] O. Dorn and D. Lesselier. Level set methods for inverse scattering. *Inverse Problems*, 22(4):67–131, 2006.

[31] H. Edelsbrunner, D. Kirkpatrick, and R. Seidel. On the shape of a set of points in the plane. *IEEE Transactions on information theory*, 29(4):551–559, 1983.

[32] C. Farhat, R. Tezaur, and R. Djellouli. On the solution of threedimensional inverse obstacle acoustic scattering problems by a regularized newton method. *Inverse Problems*, 18(5):1229–1246, 2002.

[33] E. Fernández-Cara and F. Maestre. On some inverse problems arising in elastography. *Inverse Problems*, 28(8):085001, 2012.

[34] H. P. Flath, L. C. Wilcox, V. Akçelik, J. Hill, B. van Bloemen Waanders, and O. Ghattas. Fast algorithms for bayesian uncertainty quantification in large-scale linear inverse problems based on low-rank partial hessian approximations. *SIAM Journal on Scientific Computing*, 33(1):407–432, 2011.

[35] C. Fox, H. Haario, and J. A. Christen. Inverse problems. In P. Damien, P. Dellaportas, N. G. Polson, and D. A. Stephens, editors, *Bayesian Theory and Applications*, chapter 31, pages 619–654. Oxford University Press, Oxford, 2013.

[36] C. J. Geyer. Practical markov chain monte carlo. *Statistical Science*, pages 473–483, 1992.

[37] M. Girolami and B. Calderhead. Riemann manifold langevin and hamiltonian monte carlo methods. *Journal of the Royal Statistical Society: Series B*, 73(2):123–214, 2011.

[38] J. Goodman and J. Weare. Ensemble samplers with affine invariance. *Communications in Applied Mathematics and Computational Science*, 5(1):65–80, 2010.

[39] J. F. Greenleaf, M. Fatemi, and M. Insana. Selected methods for imaging elastic properties of biological tissues. *Annual review of biomedical engineering*, 5(1):57–78, 2003.

[40] R. Griesmaier. Multi-frequency orthogonality sampling for inverse obstacle scattering problems. *Inverse Problems*, 27(8):085005, 2011.

[41] P. Hähner and T. Hohage. New stability estimates for the inverse acoustic inhomogeneous medium problem and applications. *SIAM journal on mathematical analysis*, 33(3):670–685, 2001.

[42] J. E. H. Hurtado. *Introducción al análisis estructural por elementos finitos*, volume 1.

[43] E. M. Hyde. *Fast, high-order methods for scattering by inhomogeneous media*. PhD thesis, California Institute of Technology, 2003.

[44] V. Isakov. *Inverse problems for partial differential equations*, volume 127. Springer, 2006.

[45] A. Iserles. *A first course in the numerical analysis of differential equations*. Number 15. Cambridge University Press, 1996.

[46] K. Ito, B. Jin, and J. Zou. A direct sampling method to an inverse medium scattering problem. *Inverse Problems*, 28(2):025003, 2012.

[47] O. Ivanyshyn, R. Kress, and P. Serranho. Huygens' principle and iterative methods in inverse obstacle scattering. *Advances in Computational Mathematics*, 33(4):413–429, 2010.

[48] J. Kaipio and E. Somersalo. *Statistical and computational inverse problems*, volume 160. Springer Science & Business Media, 2006.

[49] A. Kalaiah and A. Varshney. Statistical point geometry. In *Proceedings of the 2003 Eurographics/ACM SIGGRAPH symposium on Geometry processing*, pages 107–115. Eurographics Association, 2003.

[50] A. Kirsch. *An introduction to the mathematical theory of inverse problems*, volume 120. Springer Science & Business Media, 2011.

[51] A. Kirsch and R. Kress. Two methods for solving the inverse acoustic scattering problem. *Inverse problems*, 4(3):749, 1988.

[52] P.-S. Koutsourelakis. A novel bayesian strategy for the identification of spatially varying material properties and model validation: an application to static elastography. *International Journal for Numerical Methods in Engineering*, 91(3):249–268, 2012.

[53] E. Kreyszig. *Introductory functional analysis with applications*, volume 1. wiley New York, 1989.

[54] V. I. Kukulin and R. S. Mackintosh. The application of inversion to nuclear scattering. *Journal of Physics G: Nuclear and Particle Physics*, 30(2):1–55, 2004.

[55] Z. C. Kuruoğlu. Finite-rank multivariate-basis expansions of the resolvent operator as a means of solving the multivariable lippmann–schwinger equation for two-particle scattering. *Few-Body Systems*, 55(11):1167–1183, 2014.

[56] S. Langdon and C.-W. S.N. A wavenumber independent boundary element method for an acoustic scattering problem. 43(6):2450–2477, 2006.

[57] D.-T. Lee and B. J. Schachter. Two algorithms for constructing a delaunay triangulation. *International Journal of Computer & Information Sciences*, 9(3):219–242, 1980.

[58] M. Levoy and T. Whitted. *The use of points as a display primitive.* University of North Carolina, Department of Computer Science, 1985.

[59] P. Li and Y. Wang. Numerical solution of an inverse obstacle scattering problem with near-field data. *Journal of Computational Physics*, 290:157–168, 2015.

[60] L. Linsen. *Point cloud representation*. Univ., Fak. für Informatik, Bibliothek, 2001.

[61] Y. Mariappan, K. Glaser, and R. Ehman. Magnetic resonance elastography: a review. *Clinical Anatomy*, 23(5):497–511, 2010.

[62] O. Marin, O. Runborg, and A.-K. Tornberg. Corrected trapezoidal rules for a class of singular functions. *IMA Journal of Numerical Analysis*, 34(4):1509–1540, 2013.

[63] P. Neal and G. Roberts. Optimal scaling for partially updating mcmc algorithms. *The Annals of Applied Probability*, 16(2):475–515, 2006.

[64] A. Palafox, M. Capistrán, and J. A. Christen. Point cloud-based scatterer approximation and affine invariant sampling in the inverse scattering problem. *Mathematical Methods in the Applied Sciences*, 40(9):3393–3403, 2017.

[65] A. Palafox, M. A. Capistrán, and J. A. Christen. Effective parameter dimension via bayesian model selection in the inverse acoustic scattering problem. *Mathematical Problems in Engineering*, 2014, 2014.

[66] M. L. Palmeri and K. R. Nightingale. Acoustic radiation force-based elasticity imaging methods. *Interface Focus*, 1(4):553–564, 2011.

[67] W.-K. Park. On the imaging of thin dielectric inclusions buried within a half-space. *Inverse Problems*, 26(7):074008, 2010.

[68] M. Pauly. *Point primitives for interactive modeling and processing of 3D geometry*. Hartung-Gorre, 2003.

[69] M. Pauly, L. P. Kobbelt, and M. Gross. Point-based multiscale surface representation. *ACM Transactions on Graphics (TOG)*, 25(2):177–193, 2006.

[70] M. Pauly, N. J. Mitra, and L. J. Guibas. Uncertainty and variability in point cloud surface data. *SPBG*, 4:77–84, 2004.

[71] T. Pavlidis. Applications of splines to shape description. In *Visual Form*, pages 431–441. Springer, 1992.

[72] E. R. Pike and P. C. Sabatier. *Scattering, Two-Volume Set: Scattering and inverse scattering in Pure and Applied Science*. Academic press, 2001.

[73] R. Potthast. A survey on sampling and probe methods for inverse problems. *Inverse Problems*, 22(2):1–47, 2006.

[74] G. O. Roberts and J. S. Rosenthal. Optimal scaling for various metropolis-hastings algorithms. *Statistical Science*, 16(4):351–367, 2001.

[75] G. O. Roberts and O. Stramer. Langevin diffusions and metropolis-hastings algorithms. *Methodology And Computing In Applied Probability*, 4(4):337–357, 2002.

[76] O. Scherzer. *Handbook of Mathematical Methods in Imaging*. Springer, 2010.

[77] S. Schindler. Model, theory, and evidence in the discovery of the dna structure. *The British Journal for the Philosophy of Science*, 59(4):619–658, 2008.

[78] C. Schwarzl, D. Watzenig, and C. Fox. Estimation of contour parameter uncertainties in permittivity imaging using mcmc sampling. In *Sensor Array and Multichannel Signal Processing Workshop, 2008. SAM 2008. 5th IEEE*, pages 446–450. IEEE, 2008.

[79] J. P. Serrano Rubio, A. Hernández Aguirre, and R. Herrera Guzmán. Sea: an evolutionary algorithm based on spherical inversions. In *Proceedings of the Companion Publication of the 2014 Annual Conference on Genetic and Evolutionary Computation*, pages 63–64. ACM, 2014.

[80] J. Sifuentes. *Preconditioned iterative methods for inhomogeneous acoustic scattering applications*. PhD thesis, Rice University, 2010.

[81] A. M. Stuart. Inverse problems: A bayesian perspective. *Acta Numerica*, 19:451–559, 2010.

[82] A. Tarantola. *Inverse Problem Theory and Methods for Model Parameter Estimation*. Society for Industrial and Applied Mathematics, 2005.

[83] W. Tobocman. Inverse acoustic wave scattering in two dimensions from impenetrable targets. *Inverse Problems*, 5(6):1131, 1989.

[84] G. Uhlmann. *Inside Out: Inverse Problems and Applications*, volume 47. Mathematical Sciences Research Institute Publications, 2003.

[85] G. Vainikko. Fast solvers of the lippmann-schwinger equation. In *Direct and inverse problems of mathematical physics*, pages 423–440. Springer, 2000.

[86] H. A. Van der Vorst and C. Vuik. The superlinear convergence behaviour of gmres. *Journal of computational and applied mathematics*, 48(3):327–341, 1993.

[87] M. Zwicker, M. Pauly, O. Knoll, and M. Gross. Pointshop 3d: An interactive system for point-based surface editing. In *ACM Transactions on Graphics (TOG)*, volume 21, pages 322–329. ACM, 2002.